

# Small Molecule Receptor Protein Tyrosine Phosphatase $\gamma$ (RPTP $\gamma$ ) Ligands That Inhibit Phosphatase Activity via Perturbation of the Tryptophan–Proline–Aspartate (WPD) Loop<sup>†</sup>

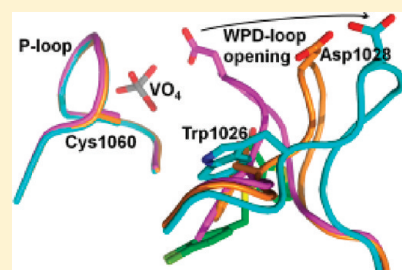
Steven Sheriff,<sup>\*,†</sup> Brett R. Beno,<sup>§</sup> Weixu Zhai,<sup>§</sup> Walter A. Kostich,<sup>§</sup> Patricia A. McDonnell,<sup>†</sup> Kevin Kish,<sup>†</sup> Valentina Goldfarb,<sup>†</sup> Mian Gao,<sup>†</sup> Susan E. Kiefer,<sup>†</sup> Joseph Yanchunas,<sup>†</sup> Yanling Huang,<sup>§</sup> Shuhao Shi,<sup>§</sup> Shirong Zhu,<sup>§</sup> Carolyn Dzierba,<sup>§</sup> Joanne Bronson,<sup>§</sup> John E. Macor,<sup>§</sup> Kingsley K. Appiah,<sup>§</sup> Ryan S. Westphal,<sup>§</sup> Jonathan O'Connell,<sup>§</sup> and Samuel W. Gerritz<sup>§</sup>

<sup>†</sup>Bristol-Myers Squibb Research and Development, P.O. Box 4000, Princeton, New Jersey 08543-4000, United States

<sup>§</sup>Bristol-Myers Squibb Research and Development, 5 Research Parkway, Wallingford, Connecticut 06492, United States

## S Supporting Information

**ABSTRACT:** Protein tyrosine phosphatases (PTPs) catalyze the dephosphorylation of tyrosine residues, a process that involves a conserved tryptophan–proline–aspartate (WPD) loop in catalysis. In previously determined structures of PTPs, the WPD-loop has been observed in either an “open” conformation or a “closed” conformation. In the current work, X-ray structures of the catalytic domain of receptor-like protein tyrosine phosphatase  $\gamma$  (RPTP $\gamma$ ) revealed a ligand-induced “superopen” conformation not previously reported for PTPs. In the superopen conformation, the ligand acts as an apparent competitive inhibitor and binds in a small hydrophobic pocket adjacent to, but distinct from, the active site. In the open and closed WPD-loop conformations of RPTP $\gamma$ , the side chain of Trp1026 partially occupies this pocket. In the superopen conformation, Trp1026 is displaced allowing a 3,4-dichlorobenzyl substituent to occupy this site. The bound ligand prevents closure of the WPD-loop over the active site and disrupts the catalytic cycle of the enzyme.



## INTRODUCTION

Protein tyrosine phosphatases (PTPs), along with protein tyrosine kinases (PTKs), play a central role in inter- and intracellular processes via phosphorylation (PTKs) and dephosphorylation (PTPs) of tyrosine residues in proteins.<sup>1–8</sup> PTPs have been implicated in a number of human diseases including various forms of cancer, diabetes, multiple sclerosis, autism, and others.<sup>1–5,7–10</sup> Therefore, considerable interest exists in PTPs as targets for pharmaceutical agents. Efforts to identify and/or design molecules that modulate the functions of various PTPs have been actively pursued.<sup>3,4,7,10–14</sup>

RPTP $\gamma$  is a member of the receptor-like (RPTP) class of protein tyrosine phosphatases. It is a type 1 integral membrane protein comprising an extracellular receptor-like domain, a region containing a catalytic PTP domain proximal to the membrane, and a catalytically inactive PTP-fold domain distal to the membrane.<sup>15</sup> Although RPTP $\gamma$  has not been studied extensively, literature reports suggest a connection between RPTP $\gamma$  and certain types of cancer.<sup>16–20</sup> In addition, disruption of the RPTP $\gamma$  gene with a  $\beta$ -galactosidase reporter gene revealed that this tyrosine phosphatase is predominantly expressed in pyramidal and sensory neurons and may serve as a marker for these neurons.<sup>21</sup> In this report, subtle behavioral changes were noted including enhanced prepulse inhibition and longer latency to first immobilization in tail suspension.<sup>21</sup> The phenotype in the

tail suspension model is consistent with an antidepressant-like activity. These observations suggest that RPTP $\gamma$  may be a worthwhile target for drug discovery efforts.

The WPD-loop (Trp-Pro-Asp), which is one of the characteristic structural motifs found in PTPs, contains an aspartic acid residue that plays a central role in the dephosphorylation mechanism.<sup>22</sup> In PTPs, the WPD-loop adopts distinctly different conformations in the presence or absence of bound peptide or small molecule ligands [cf. PTP1B X-ray crystal structures 2HNP<sup>23</sup> and 1PTY<sup>24</sup> in the Protein Data Bank (PDB)].<sup>25</sup> With no ligand bound in the active site, the WPD-loop in PTPs typically adopts an “open” conformation as exemplified by 2HNP. In comparison, ligand-bound PTPs usually assume a “closed” WPD-loop conformation as in structure 1PTY. Although the open and closed conformations are perceived to be the relevant ones in the catalytic cycle, other conformations of the WPD-loop have been reported, e.g., an intermediate<sup>26</sup> between the open and closed conformations and “atypical” conformations,<sup>27</sup> where the WPD-loop in the open position is shifted laterally.

The “closed” or active conformation of PTPs may be an unsuitable target for drug development because of difficulties

Received: March 31, 2011

Published: September 01, 2011

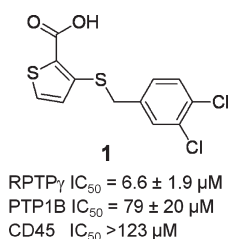


**Figure 1.** Chemical structure and measured IC<sub>50</sub> values for HTS hit compound 1.

arising from (1) the high degree of identity in the active site among PTPs and (2) the limited ability of ligands bound to the active site to access adjacent sites that do differ.

We report the discovery, biophysical characterization, and optimization of a series of small molecule RPTP $\gamma$  inhibitors that bind adjacent to the active site and perturb the WPD-loop (Trp1026-Pro1027-Asp1028) into a novel “superopen” conformation via displacement of Trp1026 from a small hydrophobic pocket. This pocket is partially occupied by Trp1026 in the open and closed enzyme conformations, while substituted aromatic moieties of bound ligands fill the pocket in the superopen conformation. Furthermore, movement of the WPD-loop into this superopen conformation modifies the shape and electrostatic characteristics of the active site. This superopen WPD-loop conformation and associated binding pocket are novel and have not been reported for other PTPs. The unique movement of the WPD-loop may be exploited to design and/or identify compounds that selectively interact with RPTP $\gamma$  relative to other PTPs. Typically, PTP active site inhibitors require acidic moieties to mimic the substrate phosphate and provide adequate affinity.<sup>3,7,10,11,13,14</sup> It may be possible to design RPTP $\gamma$  ligands with more desirable physicochemical properties by targeting the binding pocket that is exposed by the movement of the WPD-loop.

## RESULTS

We identified the initial hit, compound **1** (Figure 1), in a high throughput screen (HTS) that is described elsewhere.<sup>28</sup> Subsequently, we characterized **1** via enzyme kinetic studies, direct binding studies, and X-ray crystallography. The insights gained from the X-ray cocrystal structure and other biophysical studies of RPTP $\gamma$  with **1** facilitated the design of analogues with significantly improved in vitro activity. We also report the cocrystal structures of several key analogues with RPTP $\gamma$ .

**Characterization of the HTS Hit, Compound 1.** To support lead optimization of compound **1**,<sup>28</sup> we characterized the structure of RPTP $\gamma$  and its interactions with this HTS hit. The HTS assay used a RPTP $\gamma$  protein consisting of residues 790–1445, which is the cytoplasmic portion of the protein. This construct included domains 1 and 2 of RPTP $\gamma$ , 37 amino acids of the full length protein N-terminal to domain 1, and 16 non-native amino acids at the N-terminus.<sup>28</sup> Initial efforts to use this protein construct for structural studies met with little success. Protein recovery was poor during the buffer exchange necessary for direct binding experiments of HTS compounds, and no crystals of this protein were obtained in broad screening trials. To overcome these difficulties, a single domain 1 construct consisting of residues 825–1128 was selected for structural work.<sup>29</sup> NMR spectra of this domain 1 construct contain resonance dispersion

in both dimensions consistent with a folded protein (Figure 2a). The single isolated domain 1 protein had activity in the biological assay comparable to that of the HTS cytoplasmic protein (data not shown). This suggested that the phosphatase activity of RPTP $\gamma$  resides in domain 1, in accord with the phosphatase literature.<sup>6,8</sup>

The optimized domain 1 protein was a valuable tool for compound binding, structure determination, and activity measurements. Initial direct binding experiments consisted of NMR protein-detected experiments (transverse relaxation optimized spectroscopy, TROSY), NMR ligand-detected experiments ( $T_2$  relaxation), and a thermal shift assay.<sup>30</sup> Subsequent direct binding experiments used only the NMR protein-detected experiment. Out of ~30 HTS hits, only compound **1** exhibited direct binding using biophysical measurements. Compound **1** caused chemical shift perturbations in the <sup>1</sup>H/<sup>15</sup>N TROSY experiment of the domain 1 RPTP $\gamma$  protein (Figure 2a) and showed a drastic reduction in its  $T_2$  relaxation curve (data not shown). In addition, the melting temperature ( $T_m$ ) of the protein increased from 39.4 to 40.8 °C in the presence of **1** (100  $\mu$ M) and the  $\Delta T_m$  titrated with increasing concentrations of compound (Figure 2b). Since both NMR and thermal shift experiments indicated that **1** bound to RPTP $\gamma$ , we employed kinetic studies to further elucidate the mechanism of inhibition.

**RPTP $\gamma$ /Compound 1 Kinetic Studies.** The mechanism of RPTP $\gamma$  inhibition by **1** was characterized using a FRET-based peptide dephosphorylation assay (Z'-Lyte system). This assay used the full RPTP $\gamma$  cytoplasmic domain protein (used for the HTS screen) rather than the shorter catalytic domain protein that was used for NMR, thermal shift assay, and crystallography efforts. The kinetic parameters ( $K_m$ ,  $V_{max}$ ) of both proteins were very similar, suggesting that the absence of the C-terminal protein sequence had minimal effect on the enzymatic activity of the truncated catalytic domain protein.

Inhibition of RPTP $\gamma$  by **1** exhibited modest time dependence. A ~5-fold potency increase was observed with a 20 min compound/enzyme preincubation (IC<sub>50</sub> = 2.6 ± 0.1  $\mu$ M) relative to controls with no preincubation (IC<sub>50</sub> = 12.8 ± 0.2  $\mu$ M; see Figure 3a). Extending the preincubation to 40 min did not further improve the potency (IC<sub>50</sub> = 2.5 ± 0.1  $\mu$ M).

The reversibility of RPTP $\gamma$  inhibition by **1** was determined through comparison of progress curves from RPTP $\gamma$  pretreated with inhibitor (followed by 12-fold dilution to reduce inhibitor concentration) vs pretreatment with vehicle. The progress curves under both conditions were essentially identical, suggesting that RPTP $\gamma$  inhibition by **1** is readily reversible (Figure 3b).

The mode by which **1** inhibits RPTP $\gamma$  was determined by measuring initial velocity as a function of substrate concentration at several fixed concentrations of inhibitor. The data were fitted to the Michaelis–Menten equation and for graphical purposes were depicted in a Lineweaver–Burke plot (Figure 4a).<sup>31</sup> Compound **1** increased the apparent  $K_m$  value without altering the apparent  $V_{max}$ , consistent with a competitive mode of action. The Lineweaver–Burke plot shows the expected characteristic intersecting Y-intercepts. The  $K_i$  from a plot of apparent  $K_m$  vs [**1**] is 2.5 ± 0.6  $\mu$ M (Figure 4b).

**X-ray Structure and SAR Insights.** *Molecular Replacement and Model Building of Apo Orthorhombic Form.* While the kinetic studies indicated that **1** inhibited RPTP $\gamma$  in an apparent competitive manner, crystal structures of RPTP $\gamma$ , both in apo form and in complex with **1** and related analogues, provided a detailed picture of the manner in which the ligands compete with

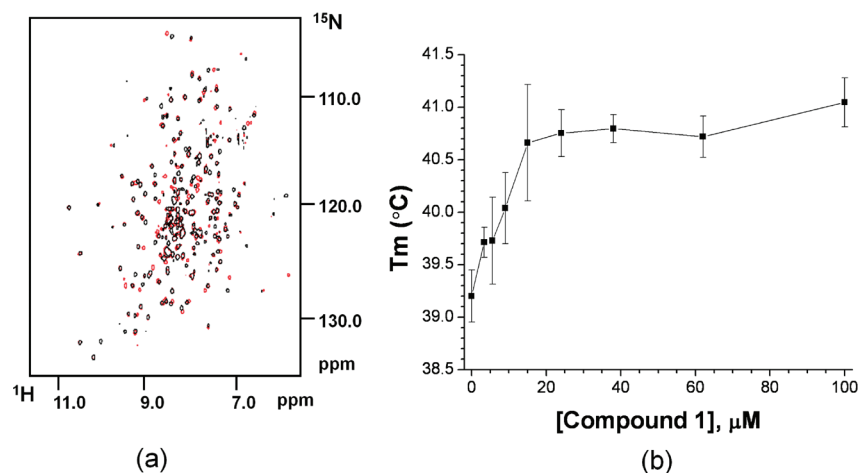


**Figure 2.** (a) Chemical shift perturbations confirm direct binding of 1 to RPTP $\gamma$ . The  $^1\text{H}/^{15}\text{N}$  TROSY NMR spectra of 125  $\mu\text{M}$  RPTP $\gamma$  (black) and upon the addition of 500  $\mu\text{M}$  of 1 (red) are shown. (b) Effect of 1 on the thermal stability of RPTP $\gamma$ . Error bars represent standard deviation from multiple replicates.

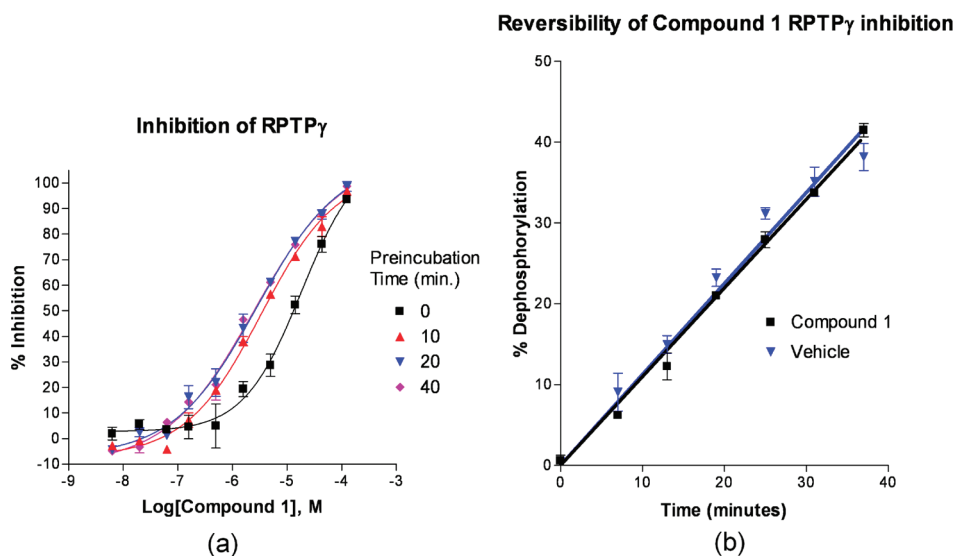


**Figure 3.** RPTP $\gamma$  inhibition by 1 is time dependent but readily reversible. (a) Compound 1 dose response curves demonstrate a preincubation time dependent increase in the potency of RPTP $\gamma$  inhibition. Compound 1 achieves maximal inhibition by the 20 min time point. The results are from a representative experiment from two trials. (b) RPTP $\gamma$  pretreated with 1 (followed by 12-fold dilution at 0 min to reduce [1]) generates an overlapping progress curve with vehicle pretreated RPTP $\gamma$ .

substrate. The first crystals obtained with the RPTP $\gamma$  domain 1 construct were orthorhombic with two molecules per asymmetric unit. As described in the methods section, molecular replacement was used with a model derived from the published RPTP $\mu$  crystal structure (1RPM).<sup>32</sup> By use of the AMoRe<sup>33–35</sup> rotation function, two peaks emerged well above the noise continuum, but 46 other peaks had heights that were at least 50% of the maximum. The two peaks did not show an obvious symmetry relationship, and both yielded clean translation function solutions. Rigid body fitting improved the statistical indicators as did combining the two solutions. The statistical indicators for molecular replacement were correlation coefficients on F and I, respectively, of 0.523 and 0.569, and the *R*-value was 0.436. Following a round of refinement, model completion proceeded and the following sequence stretches between 825 and 1128

could be traced: A chain, 825–897, 901–1000, 1014–1122; B chain, 826–898, 901–1002, 1013–1122. The chains were quite similar to each other with an rmsd of 0.6 Å for 282 of 283 *C $\alpha$*  atom pairs. Both chains resembled a typical PTP domain with an rmsd of 1.3 Å for 277 of 278 *C $\alpha$*  atom pairs relative to RPTP $\mu$  and an rmsd of 1.6 Å for 269 of 281 *C $\alpha$*  atom pairs relative to PTP1B (2HNP).<sup>23</sup>

The orthorhombic apo crystals were grown in the presence of ammonium sulfate. Sulfate anions were localized to the PTP active site, which is defined by Cys1060 in RPTP $\gamma$ . Other residues that make up the active site binding pocket include Ser1061, Ala1062, Gly1063, Val1064, and Arg1066. While this work was underway, an apo structure of domain 1 of RPTP $\gamma$  (2H4V) in a crystal form that is very similar to this structure and a structure of domain 1 and domain 2 (2NLK) were deposited.<sup>27</sup>

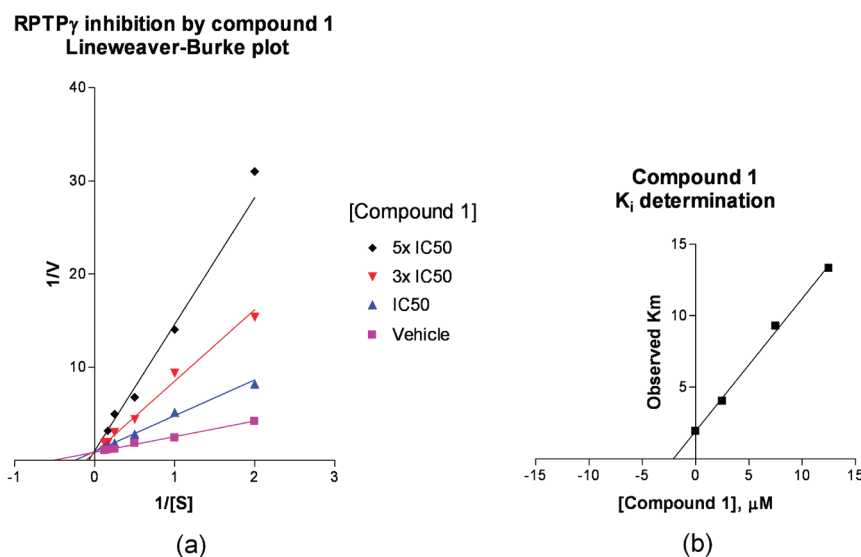


**Figure 4.** (a) Lineweaver–Burke plot for RPTP $\gamma$  inhibition by **1**. (b)  $K_i$  determination for inhibition of RPTP $\gamma$  by **1**. The results are from a representative experiment from two trials.

In the latter structure, domain 1 is similar to our apo structure of domain 1. Another RPTP $\gamma$  domain 1 structure with sulfate bound in the active site was also reported (2PBN)<sup>36</sup> and is very similar to our apo structure.

**Molecular Replacement and Model Building of Vanadate Complex.** Both orthorhombic crystals and crystals of a second, trigonal crystal form of RPTP $\gamma$ , which contained only one molecule in the asymmetric unit,<sup>29</sup> were placed in an artificial crystal growth solution containing 10 mM Na<sub>3</sub>VO<sub>4</sub>. The structure of the orthorhombic crystal form was obtained using a dimer consisting of chains A and B, and that of the trigonal crystal was determined by molecular replacement using chain A of the orthorhombic crystal form as initial models. In both crystal forms, the WPD-loop was found in the closed conformation with the vanadium atom liganded to Cys1060 S $\gamma$  and with the four oxygen atoms liganded to (1) Asp1028 O $\delta$ 1, Gln1104 N $\epsilon$ 2, and a water molecule, which was liganded to Asp1028 O $\delta$ 2; (2) Ser1061 N and Ala1062 N; (3) Gly1063 N and Val1064 N; (4) Arg1066 N and a water molecule, which was liganded to Met1029 N and Gln1108 N $\epsilon$ 2.

**Molecular Replacement and Model Building of RPTP $\gamma$  with Compound **1** Bound.** The X-ray crystal structure of the apo catalytically active phosphatase domain 1 of RPTP $\gamma$  reported here (and previously reported by other workers in PDB entries 2H4V<sup>27</sup> and 2PBN<sup>36</sup>) exhibits a WPD-loop conformation very similar to the open conformation reported for other PTPs, while the X-ray crystal structure of RPTP $\gamma$  domain 1 in complex with vanadate is in good agreement with the aforementioned closed conformation. The X-ray crystal structure of RPTP $\gamma$  domain 1 complexed with **1** revealed an unexpected and unprecedented third conformation for the WPD-loop.

The model of the dimeric apo RPTP $\gamma$  molecule discussed above was used as an initial model for molecular replacement for the orthorhombic crystals of RPTP $\gamma$  either cocrystallized with **1** or with **1** soaked into the crystal. The electron density maps for crystals where **1** was either cocrystallized or soaked into extant crystals showed very similar electron density patterns that both differed from the apo structure. Comparison to the structure of PTP1B bound to a ligand (1PTY<sup>24</sup>) clearly showed that the

WPD-loop in the RPTP $\gamma$  complex with **1** adopted a different conformation. Moreover, although it was expected that **1** would bind at the active site, since it displayed apparent competitive kinetics, it was obvious that the ligand did not bind there; i.e., it did not overlap the position of phosphotyrosine superimposed from 1PTY.<sup>24</sup> Instead, compound **1** binds in a volume partially overlapping that occupied by part of the WPD-loop (especially the side chain of Trp1026 and the main chain of Val1031 and Pro1032) in the open conformation of RPTP $\gamma$  and forces the WPD-loop to move away from the active site into a conformation we have termed superopen. In the A chain, **1** only partially occupied the site and the rest of the time the WPD-loop was in the open conformation, whereas in the B chain, **1** appeared to bind with full occupancy affording a more well-defined electron density map (Figure 5). Residues that comprise the binding site for **1** include Ile950, Tyr1023, Trp1026, Val1031, Pro1032, Arg1066, Thr1069, Thr1070, Thr1105, Glu1107, Gln1108, and Phe1111.

As shown in Figure 6, **1** binds proximal to, but not within, the active site and does not interact with the catalytic Cys1060 residue either directly or indirectly. The dichlorophenyl moiety of **1** is completely enclosed in a hydrophobic pocket formed by Ile950, Tyr1023, Trp1026, Pro1032, Val1038, Phe1041, Val1042, Thr1069, Tyr1070, Ile1073, and Phe1111. The dichlorophenyl ring and Tyr1023 form an “edge to face”  $\pi$ -stacking interaction. The thiophene moiety of **1** forms hydrophobic contacts with side chain methylenes of Glu1107 and Gln1108 and with Val1031, Pro1032, and Phe1111. The thiophene and Phe1111 form an offset “edge to face”  $\pi$ -stacking interaction. The thiomethylene linker in **1** makes hydrophobic contacts with Trp1026, Pro1032, Val1038, Phe1111, and the side chain methylene moieties of Arg1066. Polar interactions formed between **1** and RPTP $\gamma$  domain 1 include a direct hydrogen bond to the Arg1066 guanidine moiety and a water-bridged hydrogen bond to the hydroxyl moiety of Thr1105. One of the carboxylate oxygen atoms of **1** is 3.4 Å from the side chain amide nitrogen atom of Gln1108, suggesting a relatively weak hydrogen bonding interaction.

In order for **1** to bind to RPTP $\gamma$  as described above, the WPD-loop must adopt a conformation distinct from either the open or

closed conformations of apo and vanadate-bound RPTP $\gamma$ , respectively. Comparison of the vanadate-bound, apo, and compound **1**-bound X-ray structures of RPTP $\gamma$  as shown in Figure 7 highlights the extent of this conformational change. Figure 7a depicts the displacement of Asp1028 in the middle of the WPD-loop from the closed to open conformation and the additional large shift from the open to superopen conformation. A modest change in the position of Trp1026 at the N-terminal end of the WPD-loop is observed between the closed and open

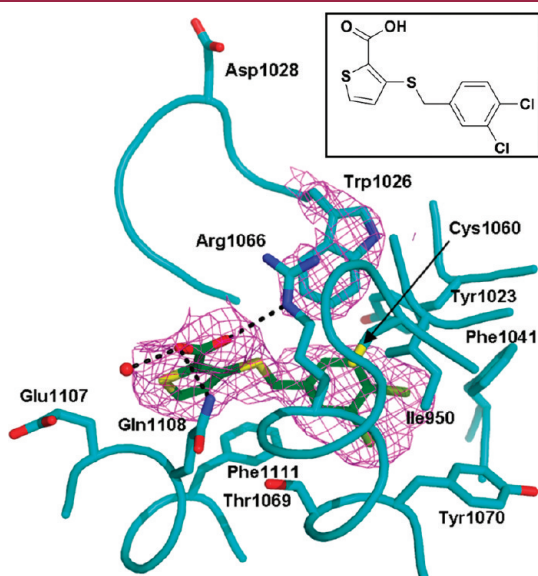


**Figure 5.** Compound **1** bound to RPTP $\gamma$ . Selected portions of RPTP $\gamma$  are shown either as a worm representing the backbone or with side chain atoms represented by sticks. RPTP $\gamma$  carbon atoms are shown in cyan. Compound **1** carbon atoms are shown in green. Nitrogen atoms are shown in blue, oxygen atoms in red, sulfur atoms in yellow, and chlorine atoms in light green. Initial (i.e., prior to fitting **1**)  $2F_o - F_c$  electron density is shown as magenta caged contours at  $1\sigma$ . Hydrogen bonds are shown in black as a series of small prolate ellipsoids. Image was created with PyMOL.<sup>37</sup>

conformations; the indole rings of Trp 1026 partially overlap (Figure 7c). However, in the compound **1**-bound superopen conformation, the indole is shifted substantially and does not overlap with the indole rings in the open and closed conformations. As shown in Figure 7b and Figure 7c, this is necessary to allow **1** to fit into the binding pocket.

These results indicate that the RPTP $\gamma$  WPD-loop can stably occupy at least three different conformations: (1) closed with traditional inhibitors, e.g., vanadate bound in the active site; (2) open with nothing other than solvent molecules, including sulfate, bound in the active site; (3) a new conformation termed superopen (Figure 7). The superopen conformation is observed when ligands such as **1** bind to a new site adjacent to the active site, displacing Trp1026. Note that Asp1028, which has been implicated in the catalytic mechanism, is distant from the active site in the open conformation and even farther away in the superopen conformation.

**Benzylthioether Analogues of 1.** Initial synthetic efforts focused on modifications to the 3,4-dichlorobenzyl thioether and carboxylic acid substituents of **1**. As shown in Table 1, the SAR of the 3,4-dichlorobenzyl thioether proved to be quite narrow and steep, particularly with respect to the position and extent of halogen substitution. For example, removal of both chloro groups of **1** afforded an inactive compound (**2**, R = Ph), while removal of the 3-chloro (**3**) or 4-chloro (**4**) substituent of **1** provided analogues with weak PTP $\gamma$  activity. Similarly, the 2,3-dichlorophenyl analogue (**5**) is 4-fold less active than **1**. Isosteric chloro replacements such as the 3,4-dimethylphenyl (**6**) and 2-naphthyl (**7**) analogues were also inactive, but the 3,4-dibromophenyl analogue **8** was equipotent with **1**, suggesting a preference for halogen substituents. Attempts to modify the thioether linker of **1** (X = S) were similarly unsuccessful, as exemplified by compounds **9** (X = O), **10** (X = NH), and **11** (X = SO<sub>2</sub>).

**Analogues of 1 That Extend into the Active Site.** In contrast to the narrow SAR observed for the 3,4-dichlorobenzyl thioether side chain, the carboxylic acid of **1** could be replaced with an acylmethylsulfonamide (**12**) or an acylphenylsulfonamide (**13**) without affecting RPTP $\gamma$  activity (Table 2). At this juncture,

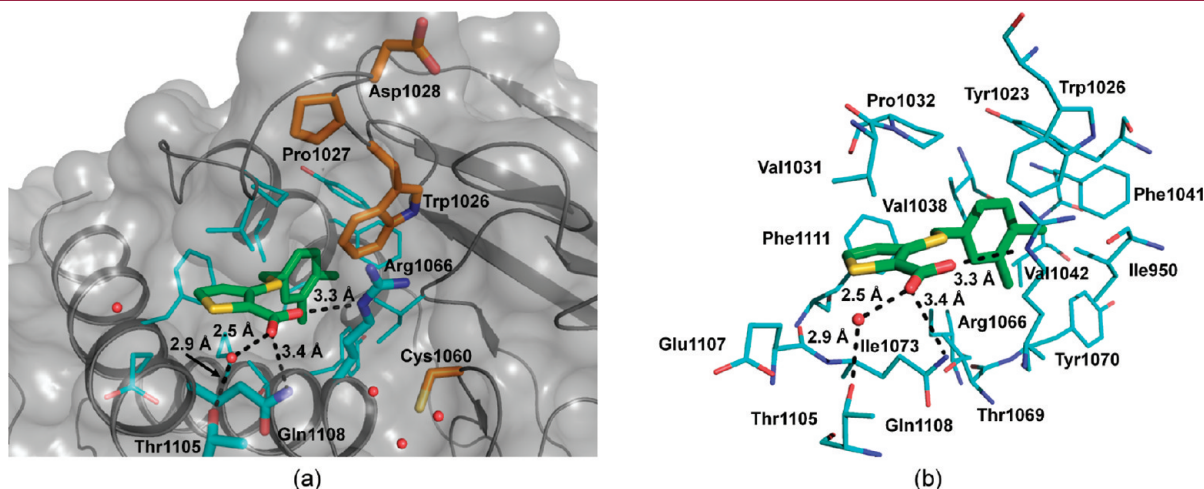


**Figure 6.** (a) Compound **1** bound to RPTP $\gamma$ . The location of the active site is indicated by Cys1060, and the Trp, Pro, and Asp residues of the WPD-loop are shown (stick representation, orange carbon atoms). Other residues proximal to the bound ligand are shown in stick representation with cyan carbon atoms, and the protein backbone is depicted with a gray cartoon representation. Water molecules are shown as red spheres, and the protein surface is shown in gray. (b) Detailed view of the binding pocket for **1** with proximal RPTP $\gamma$  residues depicted with cyan carbon atoms. Carbon atoms from **1** are in green in parts a and b. Hydrogen bonds are shown in black as a series of small prolate ellipsoids. Images were created with PyMOL.<sup>37</sup>

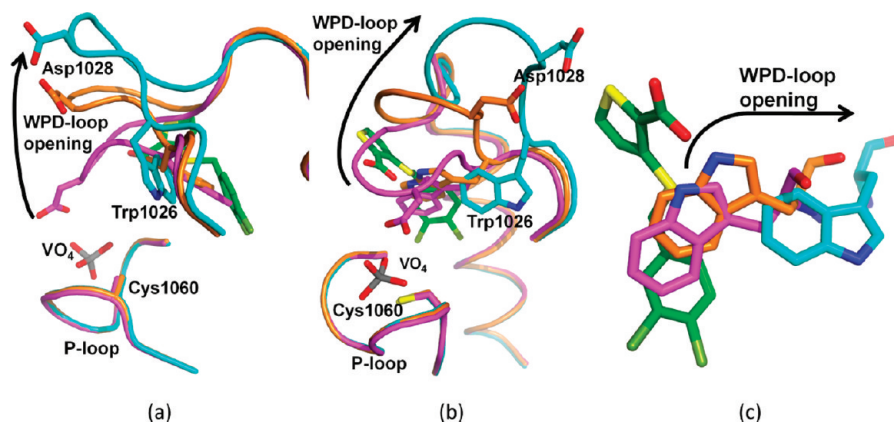
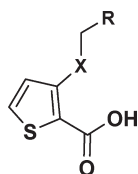


**Figure 7.** Superposition of the three states of the WPD-loop of RPTP $\gamma$ . The closed form with vanadate bound is shown in magenta. The open form of the apo protein is shown in orange, and the superopen form with **1** bound is shown in cyan. The carbon atoms for **1** are shown in green. Vanadium is shown in gray, nitrogen in blue, oxygen in red, sulfur in yellow, and chlorine in light green. (a, b) Orthogonal views in the vicinity of the binding site for **1** and the active site. (c) Close-up showing the positions of Trp1026 in the closed, open, and superopen conformations. Images were created with PyMOL.<sup>37</sup>

**Table 1.** RPTP $\gamma$  IC<sub>50</sub> for Benzylthioether Analogues of **1**

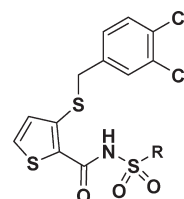


compd	R	X	IC <sub>50</sub> , $\mu$ M		
			RPTP $\gamma$	CD45	PTP1B
1	3,4-di-Cl-Ph	S	6.6	>100	79
2	Ph	S	>120	>120	50
3	4-Cl-Ph	S	80	>120	>120
4	3-Cl-Ph	S	80	>120	90
5	2,3-di-Cl-Ph	S	20	>120	40
6	3,4-di-Me-Ph	S	110	>120	>120
7	2-naphthyl	S	>120	>120	>120
8	3,4-di-Br-Ph	S	3.4	>120	60
9	3,4-di-Cl-Ph	O	>120	100	80
10	3,4-di-Cl-Ph	NH	>120	>120	>120
11	3,4-di-Cl-Ph	SO <sub>2</sub>	>120	>120	>120

the X-ray structures of **1** and **12** bound to RPTP $\gamma$  were determined and provided additional insights into analogue design. Specifically, the proximity of the binding site for **1** and **12** to the RPTP $\gamma$  active site, and the bound conformation of the acyl methylsulfonamide moiety in **12**, which directed the methyl substituent into the active site, prompted the synthesis of a number of acylphenylsulfonamide analogues. These analogues incorporated phenyl substituents capable of accepting additional hydrogen bonds from the many backbone and side chain amide NH and NH<sub>2</sub> moieties present in this region of the protein (e.g., Gln1108, Arg1066, Gln1104, Gly1065, Val1064).

Figure 8a and Figure 8b show the structures of the complexes of acylmethylsulfonamide **12** and acyl-*m*-aminophenylsulfonamide **14** bound to RPTP $\gamma$  domain 1. The thiophene and dichlorophenyl moieties of these compounds bind in a fashion similar to that described for **1** above. Similar to **1**, these compounds also form water-bridged hydrogen bonds to the side

**Table 2.** RPTP $\gamma$  IC<sub>50</sub> for Acylsulfonamide Analogues



Compound	R	RPTP $\gamma$ IC <sub>50</sub> , $\mu$ M	CD45 IC <sub>50</sub> , $\mu$ M	PTP1B IC <sub>50</sub> , $\mu$ M
12	Me	3.3	>100	73
13	Ph	3.4	48	14
14		3.8	25	81
15		0.5	>100	>100
16		5.4	73	21

chain hydroxyl moiety of Thr1105. However, they differ from each other and from **1** in how they engage Arg1066.

Compound **12** forms two hydrogen bonds to the guanidine moiety of Arg1066 through the acyl carbonyl and sulfonyl moieties. The O–N distances for both of these are relatively long, at 3.1 and 3.0 Å, respectively. The conformation of the Arg1066 side chain differs in the RPTP $\gamma$ –**14** complex, and only one, shorter (2.5 Å) and presumably stronger, hydrogen bond forms between the ligand sulfonyl group and the Arg1066 guanidine moiety. Both the methyl group in **12** and the *m*-aminophenyl moiety in **14** occupy part of the active site. However, neither the larger phenyl ring (**13**) nor the addition of the potentially hydrogen bond-donating aminophenyl moiety (**14**) provided a significant improvement in potency relative to

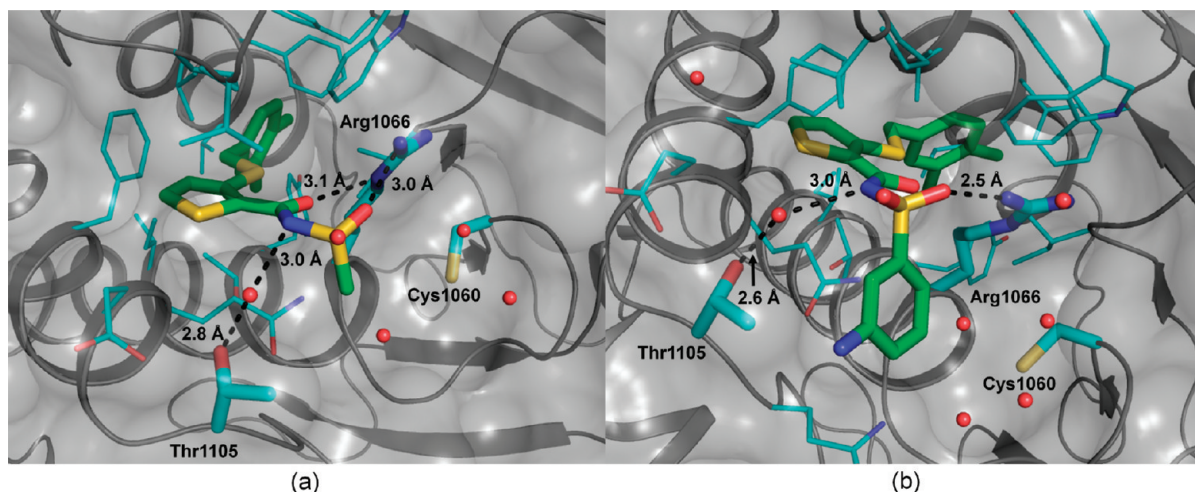


**Figure 8.** (a) Structure of the complex of RPTP $\gamma$  with acylmethylsulfonamide **12**. (b) Structure of the complex of RPTP $\gamma$  with acyl-aminophenylsulfonamide **14**. The ligands are depicted in stick representation with green carbon atoms. Residues proximal to the bound ligands are shown in stick representation with cyan carbon atoms, and the protein backbone is depicted with a gray cartoon representation. Water molecules are shown as red spheres, and the protein surface is shown in gray. Hydrogen bonds are shown in black as a series of small prolate ellipsoids. Images were created with PyMOL.<sup>37</sup>

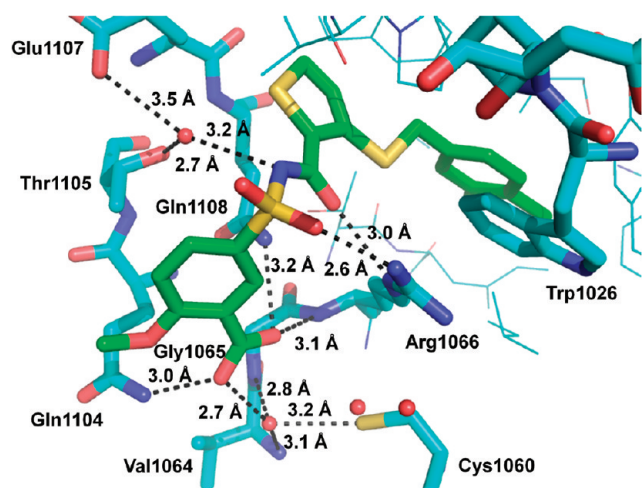


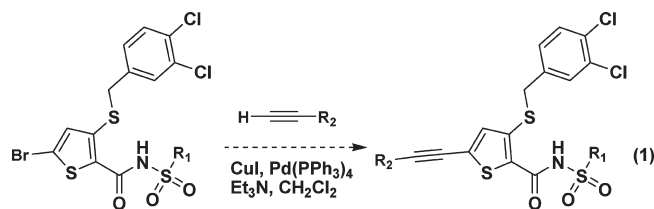
**Figure 9.** Structure of the complex of RPTP $\gamma$  with **15**. The ligand is depicted in stick representation with green carbon atoms. Residues forming direct or water-bridged hydrogen bonds to the ligand and the residues of the “WPD” motif are depicted in large diameter stick representation, and other proximal residues are depicted with thin sticks. Protein carbon atoms are colored cyan. Water molecules are shown as red spheres. Hydrogen bonds are shown in black as a series of small prolate ellipsoids. Image was created with PyMOL.<sup>37</sup>

the methyl group in **12**. As shown in Figure 8b, the amino moiety in **14** is directed away from the binding site and does not form any direct or water-bridged hydrogen bonds with the enzyme.

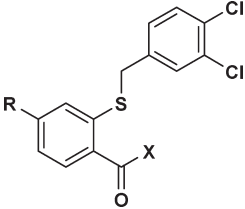
As shown in Table 2, introduction of a *m*-benzoic acid substituent (**15**) improved potency by an order of magnitude with a concomitant enhancement in selectivity versus PTP1B and a concomitant increase in the  $T_m$  from 39.4 to 44.5 °C (Supporting Information Figure S1). The corresponding methyl ester (**16**) was significantly less active, suggesting that the carboxylate was required for increased activity. This was subsequently confirmed via the X-ray structure of **15** bound to RPTP $\gamma$ . As shown in Figure 9, the acylsulfonamide moiety in **15** forms

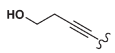
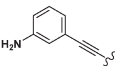
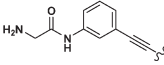
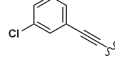
two hydrogen bonds with the Arg1066 side chain guanidine moiety, and a water-mediated hydrogen bond to Thr1105 in the same manner as **12**. The O–N distance between a side chain carboxylate oxygen atom of Glu1107 and the bridging water molecule is 3.5 Å, indicating an additional weak water-bridged hydrogen bond to the N atom of the ligand acylsulfonamide moiety. The carboxylate forms direct hydrogen bonds to the backbone NH of Arg1066 and the side chain amides of Gln1104 and Gln1108. Water-mediated interactions with the backbone NH moieties of Val1064 and Gly1065 and the SH of Cys1060 were observed as well. While the potency improvement for **15** relative to **12** was encouraging, it was achieved through the introduction of an additional acidic moiety. Since the physical properties of small molecules bearing two acidic moieties are not generally conducive to membrane permeability, as required for cellular uptake and general bioavailability, including brain uptake, additional modifications were explored.

*Analogues Reaching through “Tunnel”* Acylsulfonamide analogues such as **15** provided a significant improvement in RPTP $\gamma$  activity relative to **1**. However, substituents bearing a carboxylic acid (or bioisostere) were required to achieve submicromolar potency. Because of the need to achieve suitable druglike properties, we turned our attention to removing acidic moieties and gaining binding affinity through alternative interactions in a new pocket that we had observed in previous X-ray structures: namely, a region that is accessible via a narrow cavity or “tunnel” extending from the 5-position of the thiophene. This new region is replete with residues and affords multiple potential hydrogen bonding opportunities.



Our initial synthetic approach to 5-position analogues is shown in eq 1, wherein a 2,3,5-trisubstituted thiophene was

Table 3. RPTP $\gamma$  IC<sub>50</sub> for Alkynylbenzoic Acid Analogues


Compound	R	X	RPTP $\gamma$ IC <sub>50</sub> , $\mu$ M	CD45 IC <sub>50</sub> , $\mu$ M	PTP1B IC <sub>50</sub> , $\mu$ M
17	H	OH	5.8	>100	>100
18	H	NHSO <sub>2</sub> Me	78	>100	>100
19	Br	OH	10	>100	33
20		OH	4.0	>100	70
21		OH	5.8	>100	2.7
22		OH	1.3	>100	>100
23		OH	>100	>100	2.9

envisioned to undergo a Sonogashira reaction with a terminal alkyne to provide the corresponding alkynyl product. Unfortunately, all attempts to synthesize useful quantities of the thiophene precursor were unsuccessful, and so attention was focused on analogues of compound 17 (Table 3), in which the thiophene core was replaced by a phenyl ring. Compound 17 was equipotent with 1, but its corresponding methylacetylsulfonamide (18) was surprisingly inactive (cf. 12 and 18).

A subsequent X-ray cocrystal structure of 17 bound to RPTP $\gamma$  (Figure 10a) highlighted a major difference in the binding mode of the carboxylate compared to 1 and suggested that the corresponding acetylsulfonamide would be unable to exploit the key interactions observed in the cocrystal structure of RPTP $\gamma$  with 12. Specifically, the carboxylate of 1 is twisted out of the plane of the thiophene ring by 6°, while the carboxylate in 17 deviates from coplanarity with the attached phenyl ring by 47°. Along with other geometric differences resulting from the shapes of the five- and six-membered rings in 1 and 17, respectively, the larger deviation from coplanarity with the attached ring allows 17 to form shorter hydrogen bonds to Arg 1066 and Gln 1108 compared to 1. It also suggests that acetylsulfonamides based on 17 will not orient the sulfonamide substituent in the desired direction. As a consequence, the new vector was explored via the *p*-bromobenzoic acid analogue 19, which can be synthesized in large quantities and is an excellent substrate for the Sonogashira reaction with a variety of terminal alkynes.

As shown in Table 3, 17 and the corresponding *p*-bromo analogue 19 had similar potencies. Treatment of 19 with terminal alkynes under Sonogashira conditions yielded alkynyl analogues 20–23 and a number of interesting SAR observations. Compounds 20 and 21 provided modest improvements in potency. Compound 22 was an order of magnitude more potent than 19,

and 23 was surprisingly inactive. Compounds 21 and 23 displayed greater potency against PTP1B, one of the two PTPs employed to assess selectivity (along with CD45), than RPTP $\gamma$ . We have not determined cocrystal structures of PTP1B with any compound 1 analogues, and it is unknown how 21 and 23 bind to PTP1B.

The X-ray cocrystal structure of 20 bound to RPTP $\gamma$  was determined and is shown in Figure 10b. Although the alkynyl analogues did not provide a significant improvement in activity relative to 1, the X-ray structure of 20 bound to RPTP $\gamma$  demonstrated that additional residues proximal to the enzyme active site (e.g., Tyr841, Ile1110, Asp1114) could be targeted via substituents on the 2-(3,4-dichlorobenzylthio)benzoic acid core (17) that projected through “the tunnel” as predicted.

## DISCUSSION

NMR and thermal shift studies confirmed that 1, which was identified through high-throughput screening, binds to RPTP $\gamma$  domain 1. This ligand inhibits RPTP $\gamma$ -catalyzed dephosphorylation of substrate, and kinetic studies indicate that the mode of inhibition is apparent-competitive. Determination of the cocrystal structure of 1 with RPTP $\gamma$  revealed a new and unique hydrophobic ligand binding site on the surface of RPTP $\gamma$  domain 1 which is exposed by movement of the WPD-loop into a novel superopen conformation. This site is adjacent to the enzyme active site and is occupied by the Trp1026 side chain in the typical open and closed conformations of the enzyme. Compound 1 binds in this pocket, and when bound, it prevents the WPD-loop from closing over the enzyme active site. Residue Asp1028 from the WPD-loop is involved in the catalytic mechanism of PTPs, and thus, even if substrates could bind to the RPTP $\gamma$  active site at the same time as 1, catalytic dephosphorylation of substrate should still be inhibited. Although 1 does not directly block the active site, analysis of the RPTP $\gamma$ /1 cocrystal structure reported herein supports the results of the kinetic studies that indicate apparent competitive inhibition of the enzyme reaction. The discovery that compound 1 did not bind to the active site was a surprise because we anticipated that the carboxylate would act as a phosphate mimetic as has been seen with PTP1B active site inhibitors (e.g., see Iversen et al.,<sup>38</sup> 1C86,<sup>38</sup> 1C87,<sup>38</sup> 1C88<sup>38</sup>). An attempt to locate the binding site for compound 1 in PTP1B by soaking into extant crystals did not reveal any binding, so the binding site for compound 1 and analogues in other PTPs is unclear.

Cocrystal structures of complexes of RPTP $\gamma$  with acetylsulfonamide compounds 12 and 15 also show the ligands bound to this site. The cocrystal structure of the RPTP $\gamma$ /15 complex demonstrates the possibility of designing ligands that occupy this novel pocket and project into the enzyme active site. On the basis of this finding, a lead optimization effort resulted in the synthesis of additional compounds with ~10-fold potency improvements over the original hit, 1. However, the results to date suggest that it may prove difficult to exploit interactions with binding site residues without appending moieties that impart undesirable physicochemical properties to the resultant compounds. Attempts to show significant compound mediated inhibition of PTP $\gamma$  in a cellular context were unsuccessful (data not shown). This may be due to the modest compound potency for inhibition of PTP $\gamma$  and/or the relatively poor compound membrane permeability. This difficulty has plagued previous efforts to design PTP inhibitors with druglike properties.<sup>7,10,11,13,14</sup>



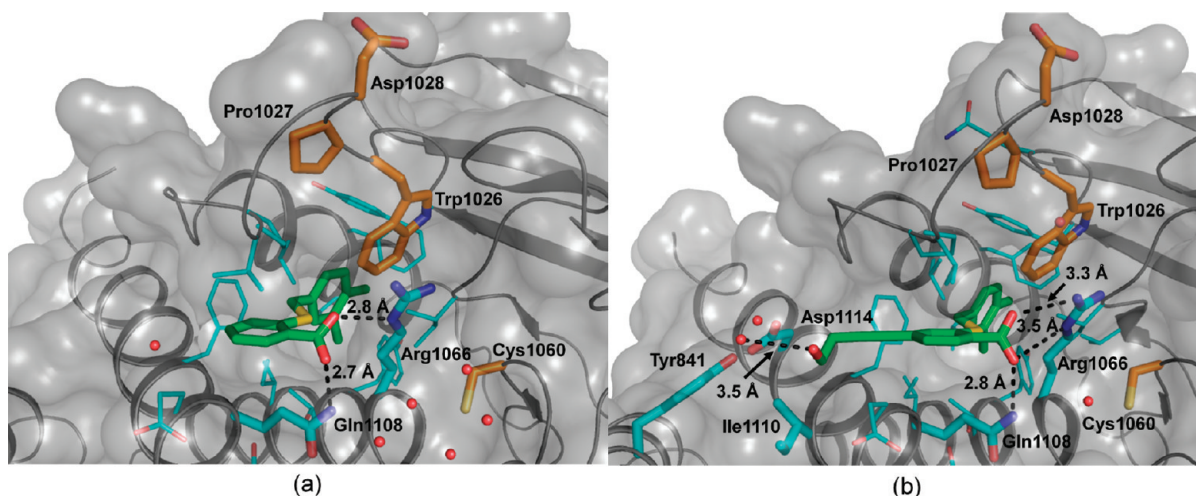


**Figure 10.** (a) Structure of the complex of RPTP $\gamma$  with 17. (b) Structure of the complex of RPTP $\gamma$  with 20. The ligands are depicted in stick representation with green carbon atoms. The location of the active site is indicated by Cys1060 which is shown in stick representation with orange carbon atoms along with the Trp, Pro, and Asp residues of the WPD-loop. Other residues proximal to the bound ligands are shown in stick representation with cyan carbon atoms, and the protein backbone is depicted with a gray cartoon representation. Water molecules are shown as red spheres, and the protein surface is shown in gray. Hydrogen bonds are shown in black as a series of small prolate ellipsoids. Image was created with PyMOL.<sup>37</sup>

While this work was in progress, the New York Structural Genomics Consortium deposited coordinates of RPTP $\gamma$  (2HY3) with vanadate bound and the WPD-loop in an open conformation.<sup>36</sup> It is unclear what might be preventing the WPD-loop from closing in that structure. The closed conformations of the WPD-loop in RPTP $\gamma$  complexed with vanadate in both crystal forms reported here were very similar, and the position of the WPD-loop resembled that for PTP1B with phosphotyrosine bound (1PTY)<sup>24</sup> rather than PTP1B with tungstate bound (2HNQ),<sup>23</sup> where it is also unclear what prevents the WPD-loop from closing. Two structures of PTP1B (3I7Z, 3I80)<sup>22</sup> with vanadate, representing two different transition state analogues for two different catalytic steps, were reported while this manuscript was in preparation. In both cases the WPD-loop is in the closed position. A search of the PDB for a sequence similar to the phosphatase domain of RPTP $\gamma$  and either tungstate or vanadate bound provided eight examples. In addition to 2HNQ<sup>23</sup> ( $\text{VO}_4^{3-}$ ) and 2HY3<sup>36</sup> ( $\text{VO}_4^{3-}$ ), which have the WPD-loop in the open conformation, and 3I7Z ( $\text{VO}_4^{3-}$ ) and 3I80 ( $\text{VO}_4^{3-}$ ), which have the WPD-loop in the closed position, four other examples were found with the WPD-loop in the closed conformation: *Yersinia* PTPase (1YTW,<sup>39</sup>  $\text{WO}_4^{3-}$ ), CDC14 (1OHD,<sup>40</sup>  $\text{WO}_4^{3-}$ ), PTP $\beta$  (2IE4,<sup>41</sup>  $\text{VO}_4^{3-}$ ), and the archaeal *Sulfolobus solfataricus* PTP (2I6M,<sup>42</sup>  $\text{VO}_4^{3-}$ ).

In a recent comprehensive analysis of PTP crystal structures, Barr and co-workers highlighted two other conformations that the WPD-loops of PTPs can adopt.<sup>27</sup> These include an “intermediate” conformation of PCPTP1 (2A8B<sup>26</sup>) in which the WPD-loop occupies a position between the open and closed states and “atypical” conformations for GLEPP1 (2GJT<sup>27</sup>), STEP (2BJJ<sup>26</sup>), and Lyp (2P6X<sup>27</sup>). In the atypical conformations, the WPD-loop moves away from the active site laterally, while the closed, intermediate, open, and superopen conformations involve more vertical displacement of the WPD-loop over the active site (Figure 11). Thus, the superopen RPTP $\gamma$  conformation reported here appears to be more related to the open, intermediate, and closed WPD-loop conformations.

The binding mode of 1 may be contrasted to that of a previously reported allosteric protein tyrosine phosphatase 1B

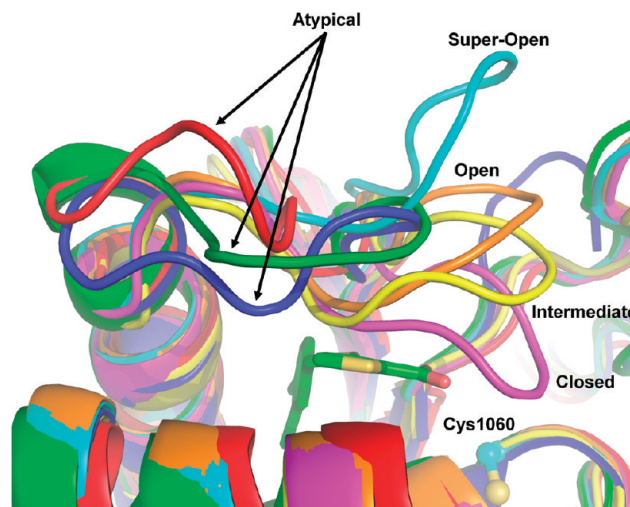


**Figure 11.** Different WPD-loop conformations of PTPs. The closed form of RPTP $\gamma$  with vanadate bound is shown in magenta. The open form with nothing bound is shown in orange, and the superopen form with 1 bound is shown in cyan. The carbon atoms for 1 are shown in green. The PTP active site is denoted by Cys1060. The intermediate WPD-loop conformation is represented by the PCPTP1 structure (2A8B,<sup>26</sup> yellow), and atypical conformations are represented by structures of GLEPP1 (2GJT,<sup>27</sup> green), STEP (2BJJ,<sup>26</sup> blue), and Lyp (2P6X,<sup>27</sup> red). Image was created with PyMOL.<sup>37</sup>

(PTP1B) inhibitor reported by Wiesmann and co-workers to inhibit PTP1B noncompetitively with respect to *p*-nitrophenyl phosphate substrate (compound 24, Figure 12).<sup>43</sup> Compound 24 binds to PTP1B at a site distant from the active site and forms multiple contacts with the protein including  $\pi$ -stacking interactions with Phe280. Based in part on a comparison of crystal structures of PTP1B with compound 24 (or close analogues) bound, PTP1B in the unliganded open conformation (2HNP<sup>23</sup>), and a Cys215Ser PTP1B mutant bound to phosphotyrosine in the closed conformation (1PTY<sup>24</sup>), Wiesmann et al. postulated

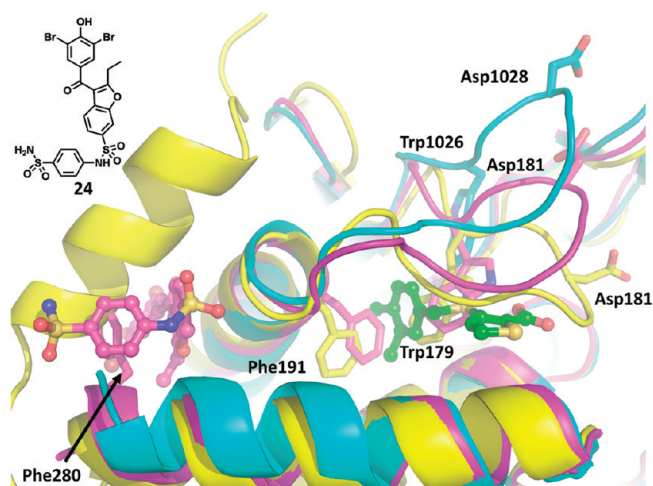


**Figure 12.** Superposition of the PTP1B/compound **24** (1T49,<sup>43</sup> magenta), the RPTP $\gamma$ /1 (cyan protein representation, ligand depicted with green carbon atoms), and the PTP1B(C215S)/pTyr (1PTY,<sup>24</sup> yellow) cocrystal structures. The Phe191 side chain in the PTP1B/compound **24** complex and **1** in the RPTP $\gamma$ /1 complex sterically hinder movement of the WPD-loop Trp side chain (Trp179 in PTP1B and Trp1026 in RPTP $\gamma$ ) to the position it occupies in the catalytically active closed conformations of the respective enzymes. The PTP WPD-closed conformation is represented by the PTP1B(C215S)/pTyr structure. Image was created with PyMOL.<sup>37</sup>

that compound **24** and analogues inhibit PTP1B by locking the enzyme in an open conformation in which the WPD-loop cannot close over the active site.<sup>43</sup> Support for this hypothesis is provided by a targeted molecular dynamics study of the complex of a compound **24** analogue with PTP1B that showed reduced WPD-loop flexibility compared to apo-PTP1B and the PTP1B-pTyr complex.<sup>44</sup> In their analysis, Wiesmann and co-workers highlighted the importance of Phe191 and pointed out that when compound **24** is bound to PTP1B, the side chain of Phe191 partially fills the cavity that Trp179 from the WPD-loop occupies in the closed conformation and prevents the WPD-loop from closing.<sup>43</sup>

Although the RPTP $\gamma$  inhibitors reported herein do not bind to RPTP $\gamma$  at a site analogous to the allosteric site where compound **24** binds to PTP1B, their putative modes of action exhibit intriguing similarities. Figure 12 shows a superposition of the RPTP $\gamma$ -1 cocrystal structure, the cocrystal structure of PTP1B with compound **24** (1T49<sup>43</sup>), and the cocrystal structure of a Cys215Ser mutant of PTP1B with phosphotyrosine bound (1PTY<sup>24</sup>). This latter structure represents a closed conformation of PTP1B. Comparison of the PTP1B/**24** and PTP1B/pTyr cocrystal structures shows that the Phe191 side chain in the PTP1B/**24** structure projects into a cavity occupied by Trp179 in the PTP1B/pTyr closed structure as originally pointed out by Wiesmann, et al.<sup>43</sup> In the RPTP $\gamma$ -1 complex, the ligand occupies part of the volume that the WPD-loop Trp1026 residue fills in the closed conformation. Thus, both the substrate non-competitive allosteric PTP1B inhibitors and the apparent-substrate-competitive RPTP $\gamma$  inhibitors reported here appear to act by perturbing the dynamics of the WPD-loop and preventing its closure over the active site. In the case of the allosteric PTP1B inhibitors, the WPD-loop is locked into a typical open conformation, while the RPTP $\gamma$  inhibitors force that enzyme into a novel superopen conformation. In both cases movement of the

WPD-loop into the closed conformation is hindered by steric interactions that prevent the Trp residue of the WPD-loop from occupying the hydrophobic pocket where it resides in the closed conformation. The different origin of the steric hindrance, direct in the case of the RPTP $\gamma$  inhibitors vs indirect (through Phe191) for the PTP1B inhibitors, may help explain the mechanistic difference (apparent competitive vs noncompetitive) between **1** and **24**.

The unique movement of the RPTP $\gamma$  WPD-loop was exploited to design compounds that were selective relative to other PTPs. Currently, the ligand-induced superopen WPD-loop conformation described herein is unique to RPTP $\gamma$ ; however, the WPD-loop is a highly conserved and mechanistically important motif in the PTP superfamily. This structural homology may portend the discovery of small molecules that inhibit other PTPs via displacement of the WPD-loop tryptophan.

## EXPERIMENTAL SECTION

**RPTP $\gamma$  Cloning and Expression.** The RPTP $\gamma$  catalytic domain construct (Figure 13) used for direct binding studies (NMR and thermal shift assay) and X-ray crystallography consisted of residues 825–1128 and is described elsewhere.<sup>29</sup> Briefly, transformed *E. coli* Rossetta (DE3) (Novagen, Madison, WI) at 37 °C were induced at OD<sub>600</sub> = 1.0 with 0.25 mM IPTG and grown for 30 h at 20 °C. The protein was isolated using ammonium sulfate precipitation, followed by Ni affinity, Q Sepharose, and SP Sepharose chromatography. The protein could be concentrated to 12 mg/mL in 25 mM Tris, pH 7.5, 200 mM NaCl, 2 mM EDTA, 5 mM DTT, and typical yields were 40 mg/L.

The RPTP $\gamma$  catalytic domain construct used for enzyme assays consisted of residues 790–1445 (full cytoplasmic domain) with an N-terminal His-myc tag. Briefly, transformed *E. coli* BL21 (DE3) growing at 37 °C were induced at OD<sub>500</sub> = 4.5 with 10% lactose and grown for 18 h at 25 °C. The cells were lysed using a MicroFluidizer, and the protein was isolated using Ni affinity and gel filtration (Superdex 75) chromatography. Finally the purified protein was dialyzed into 20 mM HEPES, pH 8.0, 200 mM NaCl, 5 mM DTT, and 40% glycerol.

**Protein Crystallization.** The purification and crystallization of the catalytic domain of RPTP $\gamma$  have been described in detail elsewhere.<sup>29</sup> Briefly, a construct was designed that encompassed residues 825–1128 of RPTP $\gamma$  and an N-terminal His<sub>6</sub> tag (Figure 13). The protein was expressed in *E. coli*. RPTP $\gamma$  was purified by sequential column chromatography involving Ni affinity, ion exchange, and molecular sieves.

Two crystal forms were examined in detail, one with symmetry consistent with space group  $P2_12_12_1$  and unit cell parameters of  $a \approx 75 \pm 1 \text{ \AA}$ ,  $b \approx 80 \pm 2.5 \text{ \AA}$ ,  $c \approx 125 \pm 2.5 \text{ \AA}$ , which had two catalytic domains per asymmetric unit. In particular, the  $b$  and  $c$  axes of this crystal form varied depending upon whether or not a ligand was bound and at which site binding occurred. A second crystal form had symmetry consistent with space group  $P3_221$  and unit cell parameters of  $a = b \approx 75 \text{ \AA}$ ,  $c \approx 152 \pm 1.5 \text{ \AA}$ . The  $c$ -axis of this crystal form varied depending upon whether or not a ligand was bound and at which site binding occurred.

**Data Collection and Processing.** Data were collected either in the laboratory or at APS ID17 (IMCA-CAT) and are reported in detail elsewhere.<sup>29</sup>

**Structure Determination by Molecular Replacement.** The CCP4<sup>33</sup> version of AMoRe<sup>34,35</sup> was used to determine the structure of RPTP $\gamma$ . The probe model used to determine the structure of the “apo” form by molecular replacement was derived from RPTP $\mu$  (1RPM).<sup>32</sup> Stretches of residues, i.e., principally loops that were thought to differ between RPTP $\mu$  and RPTP $\gamma$ , were removed. The remaining nonidentical residues from 1RPM were shorn to their minimal isostructural component, e.g., typically alanine, but for example, if RPTP $\mu$  had Phe

MGSSHHHHH SSGLVPRGSH MGSMEAIPVK QFVKHIGELY SNNQHGFSED  
 FEEVQRCTAD MNITAEHSNH PENKHKNRYI NILAYDHSRV KLRPLPGKDS  
 KHSYINANY VDGYNKAKAY IATQGPKLST FEDFWRMIWE QNTGIIVMIT  
 NLVEKGRRC K DQYWPTENSE EYGNIIIVTLK STKIHACYTV RRFSSIRNTKV  
 KKGQKGNPKG RQNERVVIQY HYTQWPDMGV PEYALPVLTF VRRSSAARMP  
 ETGPVLVHCS AGVGRGTGYI VIDSMLQIQI DKSTVNVLGF LKHIRTQRNY  
 LVQTEEQYIF IHDALLEAIL GKETEVS

**Figure 13.** Amino acid sequence of the His-Tb-RPTP $\gamma$  construct used to produce protein for NMR and crystallization studies. The hexa-His tag and the thrombin cleavage site are underlined, and the amino acids from residues 825 and 1128 of RPTP $\gamma$  are not underlined.

and RPTP $\gamma$  had Tyr at a particular position, then Phe would have been used in the model. A FORTRAN program, COALESCE, was written to bring the individual molecular replacement solutions for the orthorhombic crystal, which had two molecules in the asymmetric unit, close together in space. Following molecular replacement and interspersed with refinement and model-building, the CCP4<sup>33</sup> programs NCSMASK and DM were used for NCS map averaging and other density modifications.

**Fitting and Refinement of the Model.** CNX<sup>45</sup> (release 2005; Accelrys, Inc., San Diego, CA, U.S.) was used for refinement, and the QUANTA Modeling Environment (release 2005; Accelrys, Inc., San Diego, CA, U.S.) was employed for model fitting. In the later stages (compounds **20** and **S2**) BUSTER/TNT<sup>46</sup> was used for refinement and COOT for model fitting.<sup>47,48</sup> Figures were generated with PyMOL.<sup>37</sup>

**Direct Binding Assays.** Uniformly <sup>2</sup>H/<sup>15</sup>N labeled RPTP $\gamma$  (825–1128) for 2D TROSY experiments was expressed in minimal medium supplemented with <sup>2</sup>H glucose, <sup>15</sup>N ammonium sulfate, and 98% D<sub>2</sub>O. All samples were approximately 500  $\mu$ L in a 5 mm NMR tube. The <sup>1</sup>H/<sup>15</sup>N 2D TROSY experiments were carried out at 20 °C on a Bruker NMR spectrometer (operating at a 700 MHz <sup>1</sup>H frequency) equipped with a Bruker 5 mm <sup>1</sup>H/<sup>13</sup>C/<sup>15</sup>N triple resonance, triple-axis PFG probe. The samples were typically 125  $\mu$ M <sup>2</sup>H/<sup>15</sup>N RPTP $\gamma$ , 500  $\mu$ M compound in 50 mM sodium phosphate, pH 7.2, 100 mM NaCl, 2 mM dithiothreitol-*d*<sub>10</sub>, 1 mM EDTA-*d*<sub>16</sub>, 7% D<sub>2</sub>O.

For the NMR *T*<sub>2</sub> relaxation experiments, two samples were prepared. One sample contained ligand alone at 50  $\mu$ M, and the other sample contained 50  $\mu$ M ligand + 20  $\mu$ M RPTP $\gamma$  in 20 mM Hepes-*d*<sub>18</sub>, pD 6.8, 50 mM NaCl, 5 mM DTT-*d*<sub>10</sub>, 0.5 mM EDTA-*d*<sub>16</sub>, 1.0% DMSO-*d*<sub>6</sub>, 99% D<sub>2</sub>O. A 50 ms spin-lock time with 512 scans was collected.

The effect of inhibitors on the thermal stability of RPTP $\gamma$  was measured with a ThermoFluor instrument (3-Dimensional Pharmaceuticals, Inc. Yardley, PA)<sup>49,50</sup> by monitoring the fluorescence enhancement of an external probe (1-anilino-8-naphthalene sulfonate [ANS]), as it binds preferentially to the unfolded protein. Fluorescence was monitored with a digital camera equipped with a 500  $\pm$  30 nm filter for detection. The unfolding reactions were carried out in a 384-well plate in 5  $\mu$ L volume with 0.2 mg/mL RPTP $\gamma$  (5  $\mu$ M), 100  $\mu$ M ANS, and 2.5% (v/v) DMSO in buffer containing 25 mM PIPES, pH 7.0, 200 mM NaCl, 5 mM MgCl<sub>2</sub>, and 1 mM  $\beta$ -mercaptoethanol. The contents were overlaid with 3  $\mu$ L of polydimethylsiloxane DC200 oil (Sigma) to prevent evaporation. Unfolding reactions were monitored by ramping the temperature in 1 °C increments from 25 to 80 °C with 60 s equilibration time followed by four 10 s exposures (plus one dark field image) per temperature point. An average intensity per well was calculated by integrating pixel intensities per well and averaging the four exposures. The resulting denaturation curves were analyzed with ThermoFluor analysis software (3-Dimensional Pharmaceuticals, Inc.)

to determine *T*<sub>m</sub> values (*T*<sub>m</sub>, the temperature at which the reaction was half-complete).

**RPTP $\gamma$  Enzyme Assay.** Dephosphorylation of phosphotyrosine peptide substrate was monitored using the FRET based Z'-Lyte system (Invitrogen). The assay was carried out in a total volume of 12  $\mu$ L in a buffer containing 25 mM MOPS, 50 mM NaCl, 0.5 mM EDTA, 1 mM DTT, 0.1% Pluronic acid F-68, and 30 pM RPTP $\gamma$  full length cytoplasmic domain. Inhibitors were dissolved and serially diluted in DMSO. They were carried through a buffer intermediate dilution, added to the assay, and allowed to preincubate with enzyme. For time dependence experiments preincubation times of 0, 10, 20, and 40 min were used. All other studies used a 20 min preincubation time. The final DMSO concentration in the assay was 1.25%. The reaction was started with the addition of phosphotyrosine substrate, Z'-Lyte Phospho-Tyr 1 peptide (Invitrogen), and allowed to incubate at room temperature until the desired time-point within the assay linear range. For kinetic analysis these time points were 0, 3, 6, 9, and 12 min. The phosphatase reaction was terminated with the addition of 6  $\mu$ L of stop/development buffer consisting of development buffer B (Invitrogen) with 0.45 mg/mL development reagent B (Invitrogen) and 6 mM sodium vanadate. The terminated reaction mixture was incubated for 60 min at room temperature to allow development reagent B to cleave nonphosphorylated peptide. The plate was then imaged using a ViewLux plate reader (Perkin-Elmer) at an excitation wavelength of 400 nm and emission wavelengths of 460 and 530 nm. Percent phosphorylation was derived from the 460/530 emission ratio applied to a substrate phosphopeptide standard curve. Kinetic analysis was carried out using Prism 4.0 non-linear curve fitting (Graphpad).

Reversibility experiments were carried out as above with a few modifications. Assay preincubation conditions were 1 at 3  $\times$  *K*<sub>i</sub> (7.5  $\mu$ M) and RPTP $\gamma$  at 714 pM. After a 30 min preincubation the reaction was diluted 12-fold with buffer and phosphopeptide substrate was added at 3  $\times$  *K*<sub>m</sub> (6  $\mu$ M). A parallel vehicle-only control reaction was carried out as a measure of uninhibited RPTP $\gamma$  activity.

**Selectivity Assays.** Inhibitor activity was evaluated at two additional phosphatases, PTP-1B and CD45 (both from Upstate, Lake Placid, NY). The assay conditions were similar to those described above for RPTP $\gamma$  with the exception of the phosphatase enzyme concentrations. The phosphatases PTP-1B and CD45 were used at 50 and 500 pM, respectively. As with RPTP $\gamma$ , the assays were carried out using 2  $\mu$ M p-Tyr1 substrate peptide. The apparent *K*<sub>m</sub> we determined for PTP1B and CD45 was 0.5 and 2.1  $\mu$ M, respectively (data not shown).

**Analogue Synthesis.** All reactions were conducted in distilled solvents under an inert atmosphere. Unless otherwise noted, all reagents were purchased from commercial vendors and used without further purification. Samples were purified via reverse-phase HPLC chromatography, and final products were analyzed via HPLC-MS and <sup>1</sup>H

NMR. All NMR spectra were recorded on a Bruker DPX-500A or Bruker DPX-300B NMR spectrometer. Chemical shifts are expressed in parts per million ( $\delta$ ) using a residual solvent proton as a reference. LC/MS analysis was performed on Shimadzu HPLC equipped with a Micromass spectrometer: column, Luna 3.0 mm  $\times$  50 mm; gradient time, 2 min, from 0% B to 100% B (A, 95% H<sub>2</sub>O/5% ACN with 10 mM NH<sub>4</sub>OAc; B, 5% H<sub>2</sub>O/95% ACN with 10 mM NH<sub>4</sub>OAc). The purity of all compounds was  $\geq$ 95% as determined by HPLC analysis (UV detection at 220 nm).

Compound **1** [251096-84-1] was purchased from Key Organics (Cornwall, U.K., catalog no. 10G-330S). <sup>1</sup>H NMR (DMSO-*d*<sub>6</sub>)  $\delta$  7.90 (d, *J* = 5.2 Hz, 1H), 7.84 (s, 1H), 7.70 (d, *J* = 8 Hz, 1H), 7.61 (d, *J* = 8.2 Hz, 1H), 7.34 (d, *J* = 5.2 Hz, 1H), 4.53 (s, 2H). LC/MS (ESI) *m/z* 318 (M + H)<sup>+</sup>, *t*<sub>R</sub> = 0.92 min.

Compounds **2–8** were prepared as follows: To a solution of 3-mercaptothiophene-2-carboxylic acid (1.0 equiv) in DMSO were added sodium methoxide (25 wt % in methanol, 2.0 equiv) and the appropriate benzyl bromide (1.0 equiv). The resulting mixture was stirred at 25 °C for 3 h, then concentrated in vacuo and purified by reverse-phase preparative HPLC to afford the desired product.

**3-(Benzylthio)thiophene-2-carboxylic Acid (2)**. From 16 mg of 3-mercaptothiophene-2-carboxylic acid, 11.4 mg (46%) of **2** was obtained. <sup>1</sup>H NMR (MeOH-*d*<sub>4</sub>)  $\delta$  7.66 (d, *J* = 5.4 Hz, 1H), 7.45 (d, *J* = 7.4 Hz, 2H), 7.38 (t, *J* = 7.4 Hz, 2H), 7.28–7.23 (m, 1H), 7.16 (d, *J* = 5.4 Hz, 1H), 4.31 (s, 2H). LC/MS (ESI) *m/z* 251.1 (M + H)<sup>+</sup>, *t*<sub>R</sub> = 1.45 min.

**3-(4-Chlorobenzylthio)thiophene-2-carboxylic Acid (3)**. From 16 mg of 3-mercaptothiophene-2-carboxylic acid, 9.1 mg (32%) of **3** was obtained. <sup>1</sup>H NMR (MeOH-*d*<sub>4</sub>)  $\delta$  7.66 (d, *J* = 5.4 Hz, 1H), 7.44 (d, *J* = 8.4 Hz, 2H), 7.38 (d, *J* = 8.4 Hz, 2H), 7.14 (d, *J* = 5.4 Hz, 1H), 4.29 (s, 2H). LC/MS (ESI) *m/z* 284.1 (M + H)<sup>+</sup>, *t*<sub>R</sub> = 1.61 min.

**3-(3-Chlorobenzylthio)thiophene-2-carboxylic Acid (4)**. From 16 mg of 3-mercaptothiophene-2-carboxylic acid, 4.8 mg (17%) of **4** was obtained. <sup>1</sup>H NMR (MeOH-*d*<sub>4</sub>)  $\delta$  7.66 (d, *J* = 5.4 Hz, 1H), 7.48 (s, 1H), 7.38–7.26 (m, 3H), 7.14 (d, *J* = 5.4 Hz, 1H), 4.29 (s, 2H). LC/MS (ESI) *m/z* 285.1 (M + H)<sup>+</sup>, *t*<sub>R</sub> = 1.58 min.

**3-(2,3-Dichlorobenzylthio)thiophene-2-carboxylic Acid (5)**. From 16 mg of 3-mercaptothiophene-2-carboxylic acid, 9.2 mg (29%) of **5** was obtained. <sup>1</sup>H NMR (DMSO-*d*<sub>6</sub>)  $\delta$  7.69 (d, *J* = 5.4 Hz, 1H), 7.48 (d, *J* = 7.9 Hz, 2H), 7.26 (t, *J* = 7.9 Hz, 1H), 7.13 (d, *J* = 5.4 Hz, 1H), 4.48 (s, 2H). LC/MS (ESI) *m/z* 319.1 (M + H)<sup>+</sup>, *t*<sub>R</sub> = 1.68 min.

**3-(3,4-Dichlorobenzylthio)thiophene-2-carboxylic Acid (6)**. From 16 mg of 3-mercaptothiophene-2-carboxylic acid, 18.1 mg (65%) of **6** was obtained. <sup>1</sup>H NMR (MeOH-*d*<sub>4</sub>)  $\delta$  7.64 (d, *J* = 5.1 Hz, 1H), 7.21–7.15 (m, 3H), 7.09 (s, 1H), 4.22 (s, 2H), 2.26 (s, 3H), 2.25 (s, 3H). LC/MS (ESI) *m/z* 279 (M + H)<sup>+</sup>, *t*<sub>R</sub> = 0.9 min.

**3-(Naphthalen-2-ylmethylthio)thiophene-2-carboxylic Acid (7)**. From 16 mg of 3-mercaptothiophene-2-carboxylic acid, 7.5 mg (25%) of **7** was obtained. <sup>1</sup>H NMR (MeOH-*d*<sub>4</sub>)  $\delta$  7.91 (s, 1H), 7.86–7.84 (m, 3H), 7.65 (d, *J* = 5.4 Hz, 1H), 7.59 (d, *J* = 8.4 Hz, 1H), 7.50–7.48 (m, 2H), 7.21 (d, *J* = 5.4 Hz, 1H), 4.48 (s, 2H). LC/MS (ESI) *m/z* 301 (M + H)<sup>+</sup>, *t*<sub>R</sub> = 2.08 min.

**3-(3,4-Dibromobenzylthio)thiophene-2-carboxylic Acid (8)**. From 16 mg of 3-mercaptothiophene-2-carboxylic acid, 16.1 mg (40%) of **8** was obtained. <sup>1</sup>H NMR (MeOH-*d*<sub>4</sub>)  $\delta$  7.78 (d, *J* = 2.2 Hz, 1H), 7.66–7.61 (m, 2H), 7.35 (dd, *J* = 2.2, 8.2 Hz, 1H), 7.11 (d, *J* = 5.1 Hz, 1H), 4.27 (s, 2H). LC/MS (ESI) *m/z* 407 (M + H)<sup>+</sup>, *t*<sub>R</sub> = 0.94 min.

**3-(3,4-Dichlorobenzylthio)thiophene-2-carboxylic Acid (9)**. Compound **9** was prepared by analogy to compounds **2–8**, substituting methyl 3-hydroxythiophene-2-carboxylate for 3-mercaptothiophene-2-carboxylic acid as the starting material and utilizing 3,4-dichlorobenzyl bromide as the alkylating agent. The methyl ester thus obtained was hydrolyzed with 50% NaOH using the same procedure as described in step 2 of the preparation of compound **10** to afford 7.8 mg of **9** (26%, two steps). <sup>1</sup>H NMR (MeOH-*d*<sub>4</sub>)  $\delta$  7.72 (s, 1H), 7.61 (d, *J* = 5.5 Hz,

1H), 7.54 (d, *J* = 8.2 Hz, 1H), 7.43 (d, *J* = 8.2 Hz, 1H), 7.04 (d, *J* = 5.5 Hz, 1H), 5.26 (s, 2H). LC/MS (ESI) *m/z* 303 (M + H)<sup>+</sup>, *t*<sub>R</sub> = 2.01 min.

**3-(3,4-Dichlorobenzylamino)thiophene-2-carboxylic Acid (10)**. *Step 1*. To a solution of methyl 3-aminothiophene-2-carboxylate (314 mg, 1.0 equiv) and 3,4-dichlorobenzaldehyde (350 mg, 2.0 equiv) in THF (6 mL) were added dibutylchlorostannane (0.4 mL, 0.02 equiv) and phenylsilane (217  $\mu$ L, 2.2 equiv). The resulting mixture was stirred at 25 °C for 3 h. Then the solvent was removed in vacuo and the crude product was purified by preparative HPLC to afford 210 mg (33%) of the intermediate methyl 3-(3,4-dichlorobenzylamino)thiophene-2-carboxylate.

*Step 2*. To a solution of methyl 3-(3,4-dichlorobenzylamino)thiophene-2-carboxylate (78 mg) in 1.3 mL of EtOH was added 50% NaOH (aq) (0.3 mL). The mixture was heated to reflux for 1 h, then cooled to 25 °C and concentrated in vacuo. The crude product was diluted with ethyl acetate and water and acidified with 6 N HCl to pH ~3. The layers were separated, and the aqueous layer was back-extracted with EtOAc (3 $\times$ ). The combined organic extracts were dried (Na<sub>2</sub>SO<sub>4</sub>) and concentrated in vacuo to afford 59 mg (76%) of **10**. <sup>1</sup>H NMR (MeOH-*d*<sub>4</sub>)  $\delta$  7.51–7.49 (m, 1H), 7.46 (d, *J* = 5.4 Hz, 1H), 7.43 (s, 1H), 7.27–7.30 (m, 1H), 6.62 (d, *J* = 5.5 Hz, 1H), 4.52 (s, 2H). LC/MS (ESI) *m/z* 302 (M + H)<sup>+</sup>, *t*<sub>R</sub> = 1.03 min.

**3-(3,4-Dichlorobenzylsulfonyl)thiophene-2-carboxylic Acid (11)**. To a solution of **1** (7.8 mg, 1.0 equiv) in DCM (3 mL) was added *m*-chloroperbenzoic acid (57–86%, purchased from Aldrich, 15.5 mg, 2.2 equiv) at 25 °C. The resulting mixture was stirred at 25 °C for 16 h, then concentrated in vacuo and resuspended in MeOH and purified by preparative HPLC to afford 6.6 mg of **11** (77%). <sup>1</sup>H NMR (MeOH-*d*<sub>4</sub>)  $\delta$  7.74 (s, 1H), 7.61 (s, 1H), 7.49–7.48 (m, 2H), 7.32 (s, 1H), 7.24–7.23 (m, 1H), 5.01 (s, 2H). LC/MS (ESI) *m/z* 351 (M + H)<sup>+</sup>, *t*<sub>R</sub> = 0.82 min.

Compounds **12–14** and **16** were prepared as follows: To a solution of **1** (1.0 equiv) in DMF at 25 °C were added EDC (1.0 equiv), DMAP (1.0 equiv), and RSO<sub>2</sub>NH<sub>2</sub> (1.0 equiv). The resulting mixture was stirred at 25 °C for 6 h, then concentrated in vacuo and purified by reverse-phase preparative HPLC to afford the desired product.

**3-(3,4-Dichlorobenzylthio)-N-(methylsulfonyl)thiophene-2-carboxamide (12)**. From 12 mg of **1**, 4.5 mg (28%) of **12** was obtained. <sup>1</sup>H NMR (DMSO-*d*<sub>6</sub>)  $\delta$  7.70 (d, *J* = 6.5 Hz, 1H), 7.61 (s, 1H), 7.47 (d, *J* = 8.4 Hz, 1H), 7.37 (d, *J* = 6.5 Hz, 1H), 7.12 (d, *J* = 8.4 Hz, 1H), 4.29 (s, 2H), 3.21 (s, 3H). LC/MS (ESI) *m/z* 396 (M + H)<sup>+</sup>, *t*<sub>R</sub> = 0.90 min.

**3-(3,4-Dichlorobenzylthio)-N-(phenylsulfonyl)thiophene-2-carboxamide (13)**. From 14 mg of **1**, 2.6 mg (13%) of **13** was obtained. <sup>1</sup>H NMR (DMSO-*d*<sub>6</sub>)  $\delta$ : 8.07 (d, *J* = 7.7 Hz, 2H), 7.75–7.69 (m, 4H), 7.62 (d, *J* = 7.6 Hz, 2H), 7.38–7.36 (m, 2H), 7.17–7.14 (m, 2H), 4.17 (s, 2H). LC/MS (ESI) *m/z* 458 (M + H)<sup>+</sup>, *t*<sub>R</sub> = 1.10 min.

**N-(3-Aminophenylsulfonyl)-3-(3,4-dichlorobenzylthio)thiophene-2-carboxamide (14)**. From 11 mg of **1**, 5 mg (31%) of **14** was obtained. <sup>1</sup>H NMR (MeOH-*d*<sub>4</sub>)  $\delta$ : 7.79–7.77 (m, 1H), 7.54 (s, 1H), 7.45 (d, *J* = 8.4 Hz, 1H), 7.40–7.36 (m, 3H), 7.19–7.17 (m, 2H), 7.14–7.11 (m, 1H). LC/MS (ESI) *m/z* 473 (M + H)<sup>+</sup>, *t*<sub>R</sub> = 0.99 min.

**5-(N-(3-(3,4-Dichlorobenzylthio)thiophene-2-carbonyl)sulfamoyl)-2-methoxybenzoic Acid (15)**. Treatment of **16** (12 mg) with 3 M aq LiOH (15 equiv) in MeOH provided 10.5 mg (94%) of **15**. <sup>1</sup>H NMR (DMSO-*d*<sub>6</sub>)  $\delta$ : 8.22 (s, 1H), 8.08 (dd, *J* = 2.2 Hz, 7.6 Hz, 1H), 7.92 (d, *J* = 5 Hz, 1H), 7.64 (br s, 1H), 7.53 (m, 1H), 7.36 (m, 2H), 7.23 (d, *J* = 5 Hz, 1H). LC/MS (ESI) *m/z* 532 (M + H)<sup>+</sup>, *t*<sub>R</sub> = 0.82 min.

**Methyl 5-(N-(3-(3,4-Dichlorobenzylthio)thiophene-2-carbonyl)sulfamoyl)-2-methoxybenzoate (16)**. From 57 mg of **1**, 21.5 mg (23%) of **16** was obtained. <sup>1</sup>H NMR (DMSO-*d*<sub>6</sub>)  $\delta$ : 8.45 (s, 1H), 8.22 (dd, *J* = 2.4 Hz, 8.8 Hz, 1H), 7.75 (d, *J* = 8.0 Hz, 1H), 7.38–7.34 (m, 3H), 7.16 (m, 2H), 4.15 (s, 2H), 3.99 (s, 3H), 3.92 (s, 3H). LC/MS (ESI) *m/z* 546 (M + H)<sup>+</sup>, *t*<sub>R</sub> = 1.21 min.

2-(3,4-Dichlorobenzylthio)benzoic Acid (**17**). To a solution of 2-mercaptobenzoic acid (34.7 mg, 0.225 mmol) and 3,4-dichlorobenzyl bromide (54 mg, 0.225 mmol) in 1.2 mL of DMSO was added 0.1 mL of sodium methoxide (25 wt %, 0.45 mmol) at 25 °C. The resulting mixture was stirred at 25 °C for 6 h, then concentrated in vacuo and purified by preparative HPLC to afford 47 mg (67%) of **17**.  $^1\text{H NMR}$  (DMSO- $d_6$ )  $\delta$  7.95 (dd, 1H,  $J = 1.5$  Hz,  $J = 8.0$  Hz), 7.61 (d, 1H,  $J = 1.5$  Hz), 7.51–7.45 (m, 3H), 7.36–7.21 (m, 1H), 4.21 (s, 2H). LC/MS (ESI)  $m/z$  311 (M – H) $^-$ ,  $t_R = 0.90$  min.

2-(3,4-Dichlorobenzylthio)-*N*-(methylsulfonyl)benzamide (**18**). Compound **18** was prepared from compound **17** by analogy to the preparation of compound **12**. From 32 mg of **17**, 33 mg (81%) of **18** was obtained.  $^1\text{H NMR}$  (DMSO- $d_6$ )  $\delta$ : 7.62 (s, 1H), 7.57–7.55 (m, 2H), 7.47–7.45 (m, 2H), 7.35 (d,  $J = 8.3$  Hz, 1H), 7.31–7.28 (m, 1H), 4.24 (s, 2H). LC/MS(ESI)  $m/z$  390 (M + H) $^+$ ,  $t_R = 2.12$  min.

4-Bromo-2-(3,4-dichlorobenzylthio)benzoic Acid (**19**). Compound **19** was prepared by analogy to the preparation of compound **17**. From 4-bromo-2-mercaptobenzoic acid (387 mg, 1.66 mmol) and 3,4-dichlorobenzyl bromide (438 mg, 1.83 mmol), 480 mg (74%) of **20** was obtained.  $^1\text{H NMR}$  (MeOH- $d_4$ )  $\delta$  7.86 (d,  $J = 8.4$  Hz, 1H), 7.62 (d,  $J = 2.1$  Hz, 1H), 7.53 (d,  $J = 2.2$  Hz, 1H), 7.46 (d,  $J = 8$  Hz, 1H), 7.38 (d,  $J = 2$  Hz, 1H), 7.36 (d,  $J = 2$  Hz, 1H), 4.21 (s, 2H). LC/MS(ESI)  $m/z$  391 (M + H) $^+$ ,  $t_R = 1.08$  min.

2-(3,4-Dichlorobenzylthio)-4-(4-hydroxybut-1-ynyl)benzoic Acid (**20**). A mixture of 4-bromo-2-(3,4-dichlorobenzylthio)benzoic acid (**19**) (14.7 mg, 0.0375 mmol), but-3-yn-1-ol (5.2 mg, 0.075 mmol), tetrakis(triphenylphosphine)palladium (1 mg, 0.00087 mmol), copper(II) iodide (1 mg, 0.0053 mmol), and pyrrolidine (0.006 mL, 0.073 mmol) in H<sub>2</sub>O (1.5 mL) was heated to 70 °C for 90 min, then cooled to 25 °C, extracted with EtOAc (3 $\times$ ), dried (Na<sub>2</sub>SO<sub>4</sub>), and concentrated in vacuo to afford an oil which was purified by preparative HPLC to afford 8.8 mg (62%) of **20** as a white solid.  $^1\text{H NMR}$  (MeOH- $d_4$ )  $\delta$  7.91 (d,  $J = 8.1$  Hz, 1H), 7.61 (d,  $J = 2.2$  Hz, 1H), 7.49–7.43 (m, 2H), 7.38 (d,  $J = 2.2$  Hz, 1H), 7.36 (d,  $J = 2.2$  Hz, 1H), 7.22 (d,  $J = 7.5$  Hz, 1H), 4.20 (s, 2H), 3.75 (t,  $J = 6.6$  Hz, 2H), 2.65 (t,  $J = 6.6$  Hz, 2H). LC/MS (ESI)  $m/z$  381 (M + H) $^+$ ,  $t_R = 1.09$  min.

4-((3-Aminophenyl)ethynyl)-2-(3,4-dichlorobenzylthio)benzoic Acid (**21**). Compound **21** was prepared by analogy to the preparation of compound **20** by using 1-amino-3-ethynylbenzene as the alkyne component and triethylamine as the base. From 25 mg of 4-bromo-2-(3,4-dichlorobenzylthio)benzoic acid (**19**) (0.064 mmol), 7.1 mg (26%) of **21** was obtained.  $^1\text{H NMR}$  (DMSO- $d_6$ )  $\delta$  7.90 (d,  $J = 8.0$  Hz, 1H), 7.74 (d,  $J = 2.0$  Hz, 1H), 7.62 (d,  $J = 8.3$  Hz, 1H), 7.54 (d,  $J = 1.3$  Hz, 1H), 7.45 (dd,  $J = 8.4$ , 2.1 Hz, 1H), 7.35 (dd,  $J = 8.0$ , 1.5 Hz, 1H), 7.09 (d,  $J = 7.8$  Hz, 1H), 6.80–6.71 (m, 2H), 6.70–6.62 (m, 1H), 4.33 (s, 2H).

4-((3-(2-Aminoacetamido)phenyl)ethynyl)-2-(3,4-dichlorobenzylthio)benzoic Acid (**22**). A solution of 4-((3-aminophenyl)ethynyl)-2-(3,4-dichlorobenzylthio)benzoic acid (**21**, 4 mg, 9.34  $\mu\text{mol}$ ), Boc-Gly-OH (6.54 mg, 0.037 mmol), 2-(3H-[1,2,3]triazolo[4,5-*b*]pyridin-3-yl)-1,1,3,3-tetramethylisouronium hexafluorophosphate(V) (HATU) (5.33 mg, 0.014 mmol), and *N*-ethyl-*N*-isopropylpropan-2-amine (3.02 mg, 0.023 mmol) in 1.2 mL of NMP was stirred at 25 °C for 16 h. The product was isolated by preparative HPLC (MeOH/water with 0.1% TFA) and treated with TFA (0.1 mL, 1.3 mmol) in DCM (0.1 mL) at 25 °C for 1 h. The solvent was evaporated in vacuo to give the product 4-((3-(2-aminoacetamido)phenyl)ethynyl)-2-(3,4-dichlorobenzylthio)benzoic acid (**22**) as a TFA salt (1.5 mg, 2.5  $\mu\text{mol}$ , 30% yield over two steps).  $^1\text{H NMR}$  (MeOH- $d_4$ )  $\delta$  7.97 (d,  $J = 8.0$  Hz, 1H), 7.88 (s, 1H), 7.62 (d,  $J = 1.8$  Hz, 1H), 7.58–7.51 (m, 2H), 7.47 (d,  $J = 8.3$  Hz, 1H), 7.42–7.29 (m, 4H), 4.23 (s, 2H), 3.87 (s, 2H).

4-((3-Chlorophenyl)ethynyl)-2-(3,4-dichlorobenzylthio)benzoic Acid (**23**). Compound **23** was prepared by analogy to the preparation of compound **20** by using 1-chloro-3-ethynylbenzene as the alkyne component and triethylamine as the base. From 14.7 mg of 4-bromo-2-(3,4-

dichlorobenzylthio)benzoic acid (**19**) (0.0375 mmol), 3 mg (18%) of **23** was obtained.  $^1\text{H NMR}$  (DMSO- $d_6$ )  $\delta$  7.92 (d,  $J = 8.1$  Hz, 1H), 7.77 (d,  $J = 2.2$  Hz, 1H), 7.69 (t,  $J = 2.2$  Hz, 1H), 7.63–7.56 (m, 2H), 7.55 (t,  $J = 2.2$  Hz, 1H), 7.53 (s, 1H), 7.51–7.47 (m, 2H), 7.40 (dd,  $J = 1.5$  Hz, 8 Hz, 1H), 4.32 (s, 2H). LC/MS(ESI)  $m/z$  447 (M + H) $^+$ ,  $t_R = 1.44$  min.

## ■ ASSOCIATED CONTENT

**S Supporting Information.** Procedures for the synthesis of 3-mercaptothiophene-2-carboxylic acid and compound **1**; figure showing impact of compounds **1** and **15** on the thermal stability of RPTP $\gamma$ ; refinement statistics for X-ray crystal structures (RPTP $\gamma$  orthorhombic apo structure (PDB code 3QCB); RPTP $\gamma$  trigonal apo structure (3QCN); RPTP $\gamma$  orthorhombic vanadate complex (3QCC); RPTP $\gamma$  trigonal vanadate complex (3QCD); RPTP $\gamma$ /1 complex (3QCE, soak, 3QCF, cocrystal); RPTP $\gamma$ /S1 complex (3QCG); RPTP $\gamma$ /12 complex (3QCH); RPTP $\gamma$ /14 complex (3QCI); RPTP $\gamma$ /15 complex (3QCJ); RPTP $\gamma$ /17 complex (3QCK); RPTP $\gamma$ /20 complex (3QCL); RPTP $\gamma$ /S2 complex (3QCM)); figures showing X-ray cocrystal structures with electron density for complexes of RPTP $\gamma$  with compounds **1**, **12**, **14**, **15**, **17**, **20**, and two additional analogues. This material is available free of charge via the Internet at <http://pubs.acs.org>.

## Accession Codes

$^1\text{PDB}$  codes of RPTP $\gamma$  complexes are the following: 3QCB, 3QCC, 3QCD, 3QCE, 3QCF, 3QCG, 3QCH, 3QCI, 3QCJ, 3QCK, 3QCL, 3QCM, 3QCN.

## ■ AUTHOR INFORMATION

### Corresponding Author

\*Telephone: 609-252-5934. Fax: 609-252-6012. E-mail: [steven.sheriff@bms.com](mailto:steven.sheriff@bms.com).

## ■ ACKNOWLEDGMENT

We thank Brian Carpenter for additional cloning work, Li Tao for mass spectrometry, David Langley for generating an initial model of RPTP $\gamma$  prior to cloning and expression, and William Metzler and James Bryson for initial construct design. Use of the Advanced Photon Source (for the two vanadate structures and the compound **1** soak) was supported by the U.S. Department of Energy, Office of Science, Office of Basic Energy Sciences, under Contract No. W-31-109-Eng-38. Use of the IMCA-CAT beamline 17-ID at the Advanced Photon Source was supported by the companies of the Industrial Macromolecular Crystallography Association through a contract with the Center for Advanced Radiation Sources at the University of Chicago, IL.

## ■ ABBREVIATIONS USED

HTS, high throughput screen; PTP, protein tyrosine phosphatase; RPTP $\gamma$ , receptor protein tyrosine phosphatase  $\gamma$ ;  $T_m$ , melting temperature; TROSY, transverse relaxation optimized spectroscopy; WPD, tryptophan, proline, aspartate; DCM, dichloromethane; DMF, dimethylformamide; DMSO, dimethylsulfoxide; EtOAc, ethyl acetate; THF, tetrahydrofuran; EDC, *N*-(3-dimethylaminopropyl)-*N*-ethylcarbodiimide; DMAP, 4-dimethylaminopyridine

## REFERENCES

- (1) Alonso, A.; Sasin, J.; Bottini, N.; Friedberg, I.; Friedberg, I.; Osterman, A.; Godzik, A.; Hunter, T.; Dixon, J.; Mustelin, T. Protein Tyrosine Phosphatases in the Human Genome. *Cell* **2004**, *117*, 699–711.
- (2) Andersen, J. N.; Jansen, P. G.; Echwald, S. M.; Mortensen, O. H.; Fukuda, T.; Del Vecchio, R.; Tonks, N. K.; Moller, N. P. H. A Genomic Perspective on Protein Tyrosine Phosphatases: Gene Structure, Pseudogenes, and Genetic Disease Linkage. *FASEB J.* **2004**, *18*, 8–30.
- (3) Bialy, L.; Waldmann, H. Inhibitors of Protein Tyrosine Phosphatases: Next-Generation Drugs? *Angew. Chem., Int. Ed.* **2005**, *44*, 3814–3839.
- (4) Dewang, P. M.; Hsu, N.-M.; Peng, S.-Z.; Li, W.-R. Protein Tyrosine Phosphatases and Their Inhibitors. *Curr. Med. Chem.* **2005**, *12*, 1–22.
- (5) Hubbard, S. R.; Till, J. H. Protein Tyrosine Kinase Structure and Function. *Annu. Rev. Biochem.* **2000**, *69*, 373–398.
- (6) Taberner, L.; Aricescu, A. R.; Jones, E. Y.; Szedlacsek, S. E. Protein Tyrosine Phosphatases: Structure–Function Relationships. *FEBS J.* **2008**, *275*, 867–882.
- (7) Tautz, L.; Pellicchia, M.; Mustelin, T. Targeting the PTPome in Human Disease. *Expert Opin. Ther. Targets* **2006**, *10*, 157–177.
- (8) Tonks, N. K. Protein Tyrosine Phosphatases: From Genes, to Function, to Disease. *Nat. Rev. Mol. Cell Biol.* **2006**, *7*, 833–846.
- (9) Östman, A.; Hellberg, C.; Böhmer, F. D. Protein-Tyrosine Phosphatases and Cancer. *Nat. Rev. Cancer* **2006**, *6*, 307–320.
- (10) Vintonyak, V. V.; Antonchick, A. P.; Rauh, D.; Waldmann, H. The Therapeutic Potential of Phosphatase Inhibitors. *Curr. Opin. Chem. Biol.* **2009**, *13*, 272–283.
- (11) Combs, A. P. Recent Advances in the Discovery of Competitive Protein Tyrosine Phosphatase 1B Inhibitors for the Treatment of Diabetes, Obesity, and Cancer. *J. Med. Chem.* **2010**, *53*, 2333–2344.
- (12) Jiang, Z.-X.; Zhang, Z.-Y. Targeting PTPs with Small Molecule Inhibitors in Cancer Treatment. *Cancer Metastasis Rev.* **2008**, *27*, 263–272.
- (13) Tam, S.; Saiah, E. Recent Advances in the Discovery and Development of PTP-1B Inhibitors. *Drugs Future* **2008**, *33*, 175–185.
- (14) Zhang, S.; Zhang, Z.-Y. PTP1B as a Drug Target: Recent Developments in PTP1B Inhibitor Discovery. *Drug Discovery Today* **2007**, *12*, 373–381.
- (15) Barnea, G.; Silvennoinen, O.; Shaanan, B.; Honegger, A. M.; Canoll, P. D.; D'Eustachio, P.; Morse, B.; Levy, J. B.; LaForgia, S.; Huebner, K.; Musacchio, J. M.; Sap, J.; Schlessinger, J. Identification of a Carbonic Anhydrase-like Domain in the Extracellular Region of RPTP Gamma Defines a New Subfamily of Receptor Tyrosine Phosphatases. *Mol. Cell Biol.* **1993**, *13*, 1497–1506.
- (16) LaForgia, S.; Morse, B.; Levy, J.; Barnea, G.; Cannizzaro, L. A.; Li, F.; Nowell, P. C.; Boghosian-Sell, L.; Glick, J.; Weston, A.; Harris, C. C.; Drabkin, H.; Patterson, D.; Croce, C. M.; Schlessinger, J.; Huebner, K. Receptor Protein-Tyrosine Phosphatase Gamma Is a Candidate Tumor Suppressor Gene at Human Chromosome Region 3p21. *Proc. Natl. Acad. Sci. U.S.A.* **1991**, *88*, 5036–5040.
- (17) Liu, S.; Sugimoto, Y.; Kulp, S. K.; Jiang, J.; Chang, H.-L.; Park, K.-Y.; Kashida, Y.; Lin, Y. C. Estrogenic Down-Regulation of Protein Tyrosine Phosphatase  $\gamma$  (PTP $\gamma$ ) in Human Breast Is Associated with Estrogen Receptor  $\alpha$ . *Anticancer Res.* **2002**, *22*, 3917–3923.
- (18) Liu, S.; Sugimoto, Y.; Sorio, C.; Tecchio, C.; Lin, Y. C. Function Analysis of Estrogenically Regulated Protein Tyrosine Phosphatase  $\gamma$  (PTP  $\gamma$ ) in Human Breast Cancer Cell Line MCF-7. *Oncogene* **2004**, *23*, 1256–1262.
- (19) Tsukamoto, T.; Takahashi, T.; Ueda, R.; Hibi, K.; Saito, H.; Takahashi, T. Molecular Analysis of the Protein Tyrosine Phosphatase  $\gamma$  Gene in Human Lung Cancer Cell Lines. *Cancer Res.* **1992**, *52*, 3506–3509.
- (20) van Niekerk, C. C.; Poels, L. G. Reduced Expression of Protein Tyrosine Phosphatase Gamma in Lung and Ovarian Tumors. *Cancer Lett.* **1999**, *137*, 61–73.
- (21) Lamprinou, S.; Vacaresse, N.; Suzuki, Y.; Meziane, H.; Buxbaum, J. D.; Schlessinger, J.; Harroch, S. Receptor Protein Tyrosine Phosphatase  $\gamma$  Is a Marker for Pyramidal Cells and Sensory Neurons in the Nervous System and Is Not Necessary for Normal Development. *Mol. Cell Biol.* **2006**, *26*, 5106–5119.
- (22) Brandão, T. A. S.; Hengge, A. C.; Johnson, S. J. Insights into the Reaction of Protein-Tyrosine Phosphatase 1B: Crystal Structures for Transition State Analogs of Both Catalytic Steps. *J. Biol. Chem.* **2010**, *285*, 15874–15883.
- (23) Barford, D.; Flint, A. J.; Tonks, N. K. Crystal Structure of Human Protein Tyrosine Phosphatase 1B. *Science* **1994**, *263*, 1397–1404.
- (24) Puius, Y. A.; Zhao, Y.; Sullivan, M.; Lawrence, D. S.; Almo, S. C.; Zhang, Z.-Y. Identification of a Second Aryl Phosphate-Binding Site in Protein-Tyrosine Phosphatase 1B: A Paradigm for Inhibitor Design. *Proc. Natl. Acad. Sci. U.S.A.* **1997**, *94*, 13420–13425.
- (25) Berman, H. M.; Westbrook, J.; Feng, Z.; Gilliland, G.; Bhat, T. N.; Weissig, H.; Shindyalov, I. N.; Bourne, P. E. The Protein Data Bank. *Nucleic Acids Res.* **2000**, *28*, 235–242.
- (26) Eswaran, J.; von Kries, J. P.; Marsden, B.; Longman, E.; Debreczeni, J. E.; Ugochukwu, E.; Turnbull, A.; Lee, W. H.; Knapp, S.; Barr, A. J. Crystal Structures and Inhibitor Identification for PTPNS, PTPRR and PTPN7: A Family of Human MAPK-Specific Protein Tyrosine Phosphatases. *Biochem. J.* **2006**, *395*, 483–491.
- (27) Barr, A. J.; Ugochukwu, E.; Lee, W. H.; King, O. N. F.; Filippakopoulos, P.; Alfano, I.; Savitsky, P.; Burgess-Brown, N. A.; Muller, S.; Knapp, S. Large-Scale Structural Analysis of the Classical Human Protein Tyrosine Phosphatome. *Cell* **2009**, *136*, 352–363.
- (28) Appiah, K. K.; Kostich, W. A.; Gerritz, S. W.; Huang, Y.; Hamman, B. D.; Allen, J.; Zhang, W.; Lanthorn, T. H.; Albright, C. F.; Westphal, R.; Banks, M.; O'Connell, J. C. A High-Throughput Screen for Receptor Protein Tyrosine Phosphatase- $\gamma$  Selective Inhibitors. *J. Biomol. Screening* **2011**, *16*, 476–485.
- (29) Kish, K.; McDonnell, P. A.; Goldfarb, V.; Gao, M.; Metzler, W. J.; Langley, D. R.; Bryson, J. W.; Kiefer, S. E.; Carpenter, B.; Kostich, W. A.; Westphal, R. S.; Sheriff, S. Cloning, Purification, Crystallization and Preliminary X-ray Analysis of the Catalytic Domain of Human Receptor-like Protein Tyrosine Phosphatase  $\gamma$  in Three Different Crystal Forms. *Acta Crystallogr., Sect. F: Struct. Biol. Cryst. Commun.* **2011**, *67*, 768–774.
- (30) McDonnell, P. A.; Yanchunas, J.; Newitt, J. A.; Tao, L.; Kiefer, S. E.; Ortega, M.; Kut, S.; Burford, N.; Goldfarb, V.; Duke, G. J.; Shen, H.; Metzler, W.; Doyle, M.; Chen, Z.; Tarby, C.; Borzilleri, R.; Vaccaro, W.; Gottardis, M.; Lu, S.; Crews, D.; Kim, K.; Lombardo, L.; Roussel, D. L. Assessing Compound Binding to the Eg5 Motor Domain Using a Thermal Shift Assay. *Anal. Biochem.* **2009**, *392*, 59–69.
- (31) Copeland, R. A. *Enzymes: A Practical Introduction to Structure, Mechanism, and Data Analysis*; Wiley: New York, 2000.
- (32) Hoffmann, K. M. V.; Tonks, N. K.; Barford, D. The Crystal Structure of Domain 1 of Receptor Protein-Tyrosine Phosphatase  $\mu$ . *J. Biol. Chem.* **1997**, *272*, 27505–27508.
- (33) Collaborative Computational Project, Number 4. The CCP4 Suite: Programs for Protein Crystallography. *Acta Crystallogr., Sect. D: Biol. Crystallogr.* **1994**, *50*, 760–763.
- (34) Navaza, J. AMoRe: An Automated Package for Molecular Replacement. *Acta Crystallogr., Sect. A: Found. Crystallogr.* **1994**, *50*, 157–163.
- (35) Navaza, J.; Vernoslova, E. On the Fast Translation Functions for Molecular Replacement. *Acta Crystallogr., Sect. A: Found. Crystallogr.* **1995**, *51*, 445–449.
- (36) Almo, S. C.; Bonanno, J. B.; Sauder, J. M.; Emtage, S.; Dilorenzo, T. P.; Malashkevich, V.; Wasserman, S. R.; Swaminathan, S.; Eswaramoorthy, S.; Agarwal, R.; Kumar, D.; Madegowda, M.; Ragumani, S.; Patskovsky, Y.; Alvarado, J.; Ramagopal, U. A.; Faber-Barata, J.; Chance, M. R.; Sali, A.; Fiser, A.; Zhang, Z.-y.; Lawrence, D. S.; Burley, S. K. Structural Genomics of Protein Phosphatases. *J. Struct. Funct. Genomics* **2007**, *8*, 121–140.
- (37) *The PyMOL Molecular Graphics System*, version 1.2; Schrödinger, LLC: New York, NY.

(38) Iversen, L. F.; Andersen, H. S.; Branner, S.; Mortensen, S. B.; Peters, G. H.; Norris, K.; Olsen, O. H.; Jeppersen, C. B.; Lundt, B. F.; Ripka, W.; Møller, K. B.; Møller, N. P. H. Structure-Based Design of a Low Molecular Weight, Nonphosphorus, Nonpeptide, and Highly Selective Inhibitor of Protein-Tyrosine Phosphatase 1B. *J. Biol. Chem.* **2000**, *275*, 10300–10307.

(39) Fauman, E. B.; Yuvaniyama, C.; Schubert, H. L.; Stuckey, J. A.; Saper, M. A. The X-ray Crystal Structures of *Yersinia* Tyrosine Phosphatase with Bound Tungstate and Nitrate: Mechanistic Implications. *J. Biol. Chem.* **1996**, *271*, 18780–18788.

(40) Gray, C. H.; Good, V. M.; Tonks, N. K.; Barford, D. The Structure of the Cell Cycle Protein Cdc14 Reveals a Proline-Directed Protein Phosphatase. *EMBO J.* **2003**, *22*, 3524–3535.

(41) Xing, Y.; Xu, Y.; Chen, Y.; Jeffrey, P. D.; Chao, Y.; Lin, Z.; Li, Z.; Strack, S.; Stock, J. B.; Shi, Y. Structure of Protein Phosphatase 2A Core Enzyme Bound to Tumor-Inducing Toxins. *Cell* **2006**, *127*, 341–353.

(42) Chu, H.-M.; Wang, A. H.-J. Enzyme–Substrate Interactions Revealed by the Crystal Structures of the Archaeal *Sulfolobus* PTP-Fold Phosphatase and Its Phosphopeptide Complexes. *Proteins: Struct., Funct., Bioinf.* **2007**, *66*, 996–1003.

(43) Wiesmann, C.; Barr, K. J.; Kung, J.; Zhu, J.; Erlanson, D. A.; Shen, W.; Fahr, B. J.; Zhong, M.; Taylor, L.; Randal, M.; McDowell, R. S.; Hansen, S. K. Allosteric Inhibition of Protein Tyrosine Phosphatase 1B. *Nat. Struct. Mol. Biol.* **2004**, *11*, 730–737.

(44) Kamerlin, S. C. L.; Rucker, R.; Boresch, S. A Molecular Dynamics Study of WPD-Loop Flexibility in PTP1B. *Biochem. Biophys. Res. Commun.* **2007**, *356*, 1011–1016.

(45) Brünger, A. T.; Adams, P. D.; Clore, G. M.; DeLano, W. L.; Gros, P.; Grosse-Kunstleve, R. W.; Jiang, J.-S.; Kuszewski, J.; Nilges, M.; Pannu, N. S.; Read, R. J.; Rice, L. M.; Simonson, T.; Warren, G. L. Crystallography & NMR System: A New Software Suite for Macromolecular Structure Determination. *Acta Crystallogr., Sect. D: Biol. Crystallogr.* **1998**, *54*, 905–921.

(46) Blanc, E.; Roversi, P.; Vonrhein, C.; Flensburg, C.; Lea, S. M.; Bricogne, G. Refinement of Severely Incomplete Structures with Maximum Likelihood in BUSTER-TNT. *Acta Crystallogr., Sect. D: Biol. Crystallogr.* **2004**, *60*, 2210–2221.

(47) Emsley, P.; Cowtan, K. Coot: Model-Building Tools for Molecular Graphics. *Acta Crystallogr., Sect. D: Biol. Crystallogr.* **2004**, *60*, 2126–2132.

(48) Emsley, P.; Lokhamp, B.; Scott, W. G.; Cowtan, K. Features and development of Coot. *Acta Crystallogr., Sect. D: Biol. Crystallogr.* **2010**, *66*, 486–501.

(49) Carver, T. E.; Bordeau, B.; Cummings, M. D.; Petrella, E. C.; Pucci, M. J.; Zawadzke, L. E.; Dougherty, B. A.; Tredup, J. A.; Bryson, J. W.; Yanchunas, J., Jr.; Doyle, M. L.; Witmer, M. R.; Nelen, M. I.; Desjarlais, R. L.; Jaeger, E. P.; Devine, H.; Asel, E. D.; Springer, B. A.; Bone, R.; Salemme, F. R.; Todd, M. J. Decrypting the Biochemical Function of an Essential Gene from *Streptococcus pneumoniae* Using ThermoFluor Technology. *J. Biol. Chem.* **2005**, *280*, 11704–11712.

(50) Pantoliano, M. W.; Petrella, E. C.; Kwasnoski, J. D.; Lobanov, V. S.; Myslik, J.; Graf, E.; Carver, T.; Asel, E.; Springer, B. A.; Lane, P.; Salemme, F. R. High-Density Miniaturized Thermal Shift Assays as a General Strategy for Drug Discovery. *J. Biomol. Screening* **2001**, *6*, 429–440.